

## Abstract

HATHAWAY III, ALFRED GASTON. Design and Testing of a Prototype Slow Positron Beam at the NC State University PULSTAR Reactor. (Under the direction of Ayman I. Hawari.)

Slow positrons have proven to be a powerful tool for the analysis of materials. This nondestructive probe is capable of reconstructing the electronic environment below the surface of materials utilizing the conservation of energy and momentum on the annihilation quanta. Radioactive sources are capable of producing slow positron rates on the order of  $10^6$  Hz, but the pair production mechanism is necessary to produce more intense beams. The environment in the vicinity of nuclear reactor cores is capable of producing copious amounts of photons with energy above the threshold for the pair production mechanism.

MCNP simulations were performed which modeled North Carolina State University's PULSTAR reactor to calculate the photon flux above the pair production threshold energy. It was determined that the addition of cadmium to the end of the beam port would enhance the photon flux by a factor of 3. Further simulations demonstrated that core optimization could increase the flux by an additional factor of 2.

A positron beam was designed to focus positrons produced in the vicinity of the core into a solenoid which would allow transport through the biological shield. SIMION simulations were performed to demonstrate the effectiveness of the proposed beam and concluded that the beam design could focus positrons with a wide range of energies.

A prototype beam was completed and placed within a beam port of the PULSTAR reactor. Tests immediately demonstrated the production and control of slow positrons. Additional tests established the dependence of the count rate on the axial magnetic field of the solenoid, with a maximum count rate achieved by the prototype beam being  $33 \times 10^7$  slow positrons per second.

The knowledge gained from the prototype can be applied to future work to improve the overall beam effectiveness. Future works includes the bending of the solenoid and implementation of core optimizations. The size of the moderator can also be increased from that of the prototype to increase the beam intensity.

# Design and Testing of a Prototype Slow Positron Beam at the NC State University PULSTAR Reactor

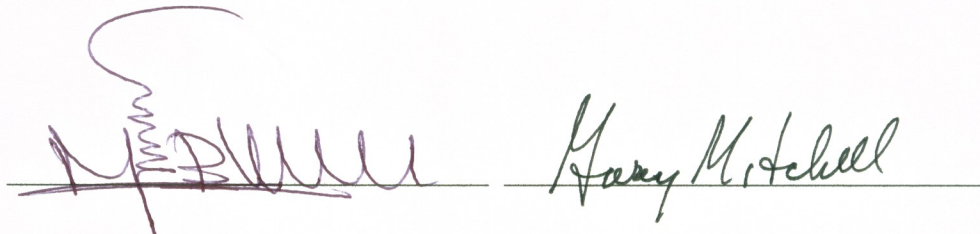
by  
**Alfred G. Hathaway III**

A thesis submitted to the Graduate Faculty of  
North Carolina State University  
in partial fulfillment of the  
requirements for the Degree of  
Master of Science

**NUCLEAR ENGINEERING**

Raleigh

2005



Chair of Advisory Committee

# Biography

Alfred Gaston Hathaway III (Trey Hathaway) was born March 3, 1981 in Greenville, North Carolina to Alfred and Gloria Hathaway. Greenville is a moderate sized city in Eastern North Carolina, home to East Carolina University and numerous industries.

In August of 1999, the author began attending North Carolina State University where he worked to obtain a degree in Chemical Engineering. Accomplishments during college include being a member of the winning design team competing in the 2003 Energy Challenge, sponsored by the United States Department of Energy. He graduated Magna Cum Laude in May of 2003.

During his senior year, the author decided to continue his education by studying Nuclear Engineering. He began his studies in August of 2003 at North Carolina State University. He began working with Dr. Ayman Hawari in MCNP modeling and radiation detection.

Over the summer of 2004, the author traveled to the University of Michigan, Ann Arbor, where he worked with the Michigan Positron Group, directed by Dr. David Gidley. It was at this time where he began to learn the background and helped in construction of components which allowed the completion of this work.

## Acknowledgements

The author would like to extend his deepest gratitude to Dr. Ayman Hawari for his guidance throughout the course of this project. He appreciates the opportunity granted to him with this project and allowing him the ability to work with so many hard working people.

He would also like to thank Dr. David Gidley, Dr. Mark Skalsey, Dr. William Frieze, Dr. Richard Vallery and all those involved with the Michigan Positron Group for their work on the prototype beam, their guidance while learning the basics of positron physics and the use of the program SIMION, and their patience throughout the data collection process. Special thanks should be extended to Dr. Mark Skalsey and Dr. David Gidley for their assistance in the editing of this completed thesis. The constructive comments offered by Dr. Jun Xu of Oak Ridge National Laboratory were also greatly appreciated.

The author would like to express his thanks to Dr. Mohamed Bourham and Dr. Gary Mitchell for agreeing to serve on this thesis committee and the guidance they offered along the way

Thanks should also be given to Dr. Jianwei Chen for his assistance with MCNP and the preliminary work performed by him while working with the Nuclear Reactor Program of North Carolina State University.

Finally, the author would like to extend his thanks to Mr. Andrew Cook, Mr. Larry Broussard, Mr. Kerry Kincaid, and all of the student operators involved for their assistance in the construction of shielding for the positron beam prototype and their patience while operating the PULSTAR reactor throughout the data collection process.

## Table of Contents

	Page
<b>List of Tables</b> .....	vi
<b>List of Figures</b> .....	vii
<b>Chapter 1 Introduction to Positron Physics</b> .....	1
1.1 Introduction.....	1
1.2 Positron Physics.....	2
1.2.1 Implantation .....	2
1.2.2 Moderation.....	4
1.2.3 Annihilation .....	5
1.2.4 Positronium.....	6
1.3 Positron Sources.....	8
1.3.1 Radioactive Sources.....	8
1.3.2 Pair Production.....	8
1.4 Positron Transport.....	9
1.4.1 Electrostatic Lenses .....	9
1.4.2 Magnetic Lenses .....	10
1.5 Detection and Uses of Positrons .....	11
1.5.1 Positron Lifetime Spectroscopy.....	11
1.5.2 Doppler Broadening.....	12
1.5.3 Angular Correlation of Annihilation Radiation .....	13
<b>Chapter 2 Prototype Design Simulations</b> .....	14
2.1 Introduction.....	14
2.2 MCNP Simulations.....	14
2.2.1 NCSU PULSTAR Reactor.....	14
2.2.2 MCNP Simulations.....	15
2.2.3 Estimation of Beam Rate .....	20
2.2.4 MCNP Optimization.....	20
2.3 SIMION Simulations .....	24
<b>Chapter 3 Construction of Prototype Slow Positron Beam</b> .....	36
3.1 Material Selection.....	36
3.2 The Moderator/Converter Assembly .....	38
3.3 Beam Design.....	41
3.3.1 Solenoid Design and Construction.....	42
3.3.2 Vacuum Chamber Design and Construction.....	46

3.3.3	Electrostatic Lens Design and Construction .....	49
3.3.4	Beam Assembly .....	52
3.4	Shielding Construction.....	53
<b>Chapter 4 Testing and Results for Prototype.....</b>		<b>62</b>
4.1	Introduction.....	62
4.2	Electronic Setup .....	62
4.3	Detection Efficiency .....	64
4.4	Initial Tests.....	66
4.5	Magnetic Transport Efficiency .....	67
4.6	Final Prototype Tests .....	73
4.6.1	Source Location Tests.....	74
4.6.2	Mapping of Residual Magnetic Field .....	76
<b>Chapter 5 Conclustions and Future Work.....</b>		<b>78</b>
5.1	Conclusion .....	78
5.2	Future Work.....	79
5.2.1	Bending of Beam .....	79
5.2.2	Remoderation.....	80
<b>References.....</b>		<b>82</b>
<b>Appendices .....</b>		<b>85</b>
Appendix A.....		86

## List of Tables

	Page
Table 2.1. Comparison of energy spectra for POSH and PULSTAR reactors .....	19
Table 2.2. Working Lens Voltages utilized in prototype beam .....	34
Table 3.1. Induced Radioactivities in the Converter/Moderator Assembly after 60 hours ....	37
Table 3.2. Maximum Induced Radioactivities in 6061 Al Alloy after 60 hours .....	37
Table 3.3. Magnetic Field and Power for Various Currents .....	46
Table 4.1. Count Rate with Differing Magnetic Field Orientation.....	69
Table A.1. Partial sorting of prompt gamma rays based on product of flux and intensity .....	87

## List of Figures

	Page
Fig. 2.1. Schematic of reactor with biological shield and beam ports .....	15
Fig. 2.2. Simulation model of PULSTAR reactor core.....	16
Fig. 2.3. Calculated photon flux across beam port 6 .....	17
Fig. 2.4. Total photon flux vs. cadmium insert thickness.....	18
Fig. 2.5. Photon flux in 1MeV energy bins of the POSH and PULSTAR reactors with the pair production cross section for tungsten .....	19
Fig. 2.6. Simulation with beryllium reflectors replacing graphite reflectors.....	21
Fig. 2.7. Simulation with beryllium reflectors and reversed core orientation .....	21
Fig. 2.8. Optimization of cadmium thickness with current core configuration and optimize orientation.....	22
Fig. 2.9. Simulation of moderator tube with five equally spaced emission points .....	26
Fig. 2.10. Histogram of possible perpendicular energy with plate potential of +40V and grid potential of -40V .....	27
Fig. 2.11. Histogram of possible perpendicular energy with plate potential of +10V and grid potential of -10V .....	28
Fig. 2.12. Histogram of possible perpendicular energy with plate potential of +80V and grid potential of -80V .....	28
Fig. 2.13. Simulation of one-third scale Delft design.....	29
Fig. 2.14. Simulation with Delft lens design with altered lens voltages.....	30
Fig. 2.15. Simulation with transport lens 4 increased to -2000V and the first lens set to -5V .....	31
Fig. 2.16. Simulation with voltages on adjacent lenses in approximate 1:4 ratio.....	32
Fig. 2.17. Series of simulation with altering emission energies; a) 3eV, b) 8eV, c) 13eV, d) 20eV, e)25eV, and f) 30eV .....	33
Fig. 2.18. Simulation of tubular lens design .....	34
Fig. 2.19. Simulation of positron focusing and transport .....	35
Fig. 3.1. Probability of occurrence of pair production event vs. incident photon energy for various elements.....	38
Fig. 3.2. Mockup of moderator/converter array.....	40
Fig. 3.3. Layout of positron beam in beam port.....	42
Fig. 3.4. Picture of winding setup.....	44
Fig. 3.5. Pump adapter .....	47
Fig. 3.6. Schematic of Delft lens design .....	50
Fig. 3.7. Schematic of lens design .....	50
Fig. 3.8. Final assembly of beam .....	53
Fig. 3.9. Empty beam port 6 .....	53
Fig. 3.10. Beam port insert on aluminum stand.....	54
Fig. 3.11. Images of the beam port insert; a) placed within the beam port, b) completed beam port insert.....	55
Fig. 3.12. Construction of base of the shielding .....	56
Fig. 3.13. Close-up of borated polyethylene layer.....	58

Fig. 3.14. Images of lead layer; a) front view, b) side view .....	59
Fig. 3.15. Images of detector placement; a) close-up, b) side view.....	60
Fig. 3.16. Initial shield setup.....	61
Fig. 3.17. Completed shield.....	61
Fig. 4.1. Schematic of slow positron detection electronics.....	62
Fig. 4.2. Coincidence spectrum taken at reactor power level of 10kW .....	63
Fig. 4.3. Count rate vs. power level .....	66
Fig. 4.4. Count rate vs. magnetic field.....	68
Fig. 4.5. Count rate vs. magnetic field in favorable and original magnetic field orientation.....	69
Fig. 4.6. Count rate vs. magnetic field with higher current levels.....	70
Fig. 4.7. Data taken which shows no trend or control .....	71
Fig. 4.8. Count rate vs. magnetic field with 2 minutes of stabilization .....	72
Fig. 4.9. Count rate vs. magnetic field with cooling periods and no stabilization.....	73
Fig. 4.10. Count rate vs. position of Ge-68 source .....	74
Fig. 4.11. Effect of solenoid heating on count rate.....	75
Fig. 4.12. Horizontal and vertical transverse and axial magnetic fields within the beam port.....	76
Fig. 5.1: Comparison of photon fluxes for current and optimized core arrangements .....	78

# Chapter 1

## Introduction to Positron Physics

### *1.1 Introduction*

In the late 1920's, Paul Dirac combined quantum mechanics and relativity to produce a thorough description of the electron. The proposed equations contained a puzzling result. Any solution which resulted in an electron with a positive energy included a counterpart where the energy was negative. Eventually it was believed that these counterpart equations corresponded to a new particle, which was analogous to the electron but had a positive charge. Dirac called this particle the "anti-electron", but soon it became known as the positron. His early predictions for this particle were that they should not be expected to be found readily in nature due to their prompt recombination with electrons but they could be produced in vacuum and prove to be quite stable and easily be observed. Dirac has been proven correct on both counts [1].

Just a few years later, in 1932, experiments performed by Charles D. Anderson brought forth evidence of an unknown particle, which was later identified as the positron [2]. The findings were supported by Blackett and Occhialini in 1933 who observed the occurrence of pair production, the creation of an electron-positron pair. It has been shown experimentally using trapped particles that the gyromagnetic ratios [3], the ratio of the magnetic dipole moment to the mechanical angular momentum of a system [4], of the electron and positron are equal within 2 parts in  $10^{12}$ . The charge is equal within 4 parts in  $10^{12}$ . It is predicted that the positron is stable in a vacuum environment, which is supported

by laboratory evidence from experiments which can trap a single positron for periods on the order of months [3].

## 1.2 Positron Physics

### 1.2.1 Implantation

Energetic positrons have the ability to implant in materials, although some are backscattered. Positron backscattering is dependent on the thickness and atomic number of the material. The implantation profile,  $P(x)$ , for beta decay positrons,  $\beta^+$ , is expressed in terms of the distance implanted,  $x$ , and an absorption coefficient,  $\mu_{imp}$ :

$$P(x) = \mu_{imp} \exp(-\mu_{imp}x) \quad (1.1)$$

The absorption coefficient is related to the maximum energy of the incident positrons and the density of the target [3]. It is possible to calculate the implantation profile for a monoenergetic beam. Using Monte Carlo techniques, the positron implantation profile can be characterized by a Makhovian profile, given by the following formula [5]:

$$P(E, z) = \frac{mz^{m-1}}{z_0^m} \exp\left(-\left(\frac{z}{z_0}\right)^m\right) \quad (1.2)$$

For this profile,  $P(E,z)dz$  is the fraction of positrons with a particular energy that are stopped between  $z$  and  $z + dz$ . The mean implantation depth of the positrons, given by [5]:

$$\bar{z} = \frac{\alpha}{\rho} E^n \quad (1.3)$$

where  $\alpha$  and  $n$  are material independent constants and  $\rho$  is the density of the material, can be related to the parameter  $z_0$  by the relationship of [5]:

$$\bar{z} = \frac{\sqrt{\pi}}{2} z_0 \quad (1.4)$$

At low energies, approximately 10-50 eV where motion ceases to be ballistic and cross sections become less accurate, Monte Carlo simulations are terminated [6].

The eventual fate of positrons within condensed matter is annihilation with an electron, the lifetime of this process being on the order of nanoseconds. During this short period of time, positrons lose energy through a variety of processes, which can be observed through the annihilation radiation. Once high energy positrons encounter condensed matter, they rapidly lose energy due to inelastic scattering, which involve electronic excitation. These processes can include core level ionization and excitation as well as valence shell interactions. At energies in the range of a few eV and below, phonon scattering begins to be seen [6].

At high energies, electrons lose their kinetic energy faster than positrons in a medium, but a crossover takes place around 100 keV. At this energy, the Bethe-Bloch depiction of stopping power becomes valid [6] which represents the scattering of charged particles off atomic electrons [7]. Electrons can only lose half of their incoming energy due to the fact that they are indistinguishable from target electrons. Because differences arise between electrons and positrons in regards to exchange symmetry, it is to be expected that positrons will lose their energy slightly faster [6].

Once positrons reach a cutoff energy of 10-50 eV, they travel as epithermal particles. If kinetic energies incident on a material are low, positrons can possibly escape the surface before they fully thermalize [6], or reach the average energy of the medium, given by  $3k_bT/2$  [5].

The energy loss mechanism of phonon excitations take over at low energies to reduce the kinetic energy from eV to thermal energies. The most important mode is that of longitudinal acoustic vibrations [6]. Positrons come to thermal energies within a few picoseconds at thermal room temperatures. At these energies, positrons continue to travel via quantum diffusion processes. Positrons are capable of being trapped in attractive potential wells, regions of low atomic density, such as lattice defects in crystals. Charged impurities can also trap positrons at low energies [6]. Motion is considered to be a homogeneous random walk and over lengths which are longer than the mean free path of the positron, the motion can be considered to be diffusive. The continuity equation for positrons is shown below:

$$\frac{\partial n(x,t)}{\partial t} + \nabla \cdot \vec{J}(x,t) = -\lambda(x)n(x,t) \quad (1.5)$$

where  $n(x,t)$  is the time dependent density of the positrons,  $J(x,t)$  is the current density and  $\lambda(x)$  is the depletion rate of the diffusing positrons. The value of  $\lambda(x)$  must therefore be the sum of the rates of removal by annihilation,  $\lambda_{ann}$ , and removal by trapping,  $\kappa(x)$ :

$$\lambda(x) = \lambda_{ann} + \kappa(x) \quad (1.6)$$

The diffusion of the positrons is then described by Fick's law, which will include a term to compensate for the electric field, if one is present:

$$\vec{J}(x,t) = -D_+ \nabla n(x,t) + \eta_+ \vec{E}(x) \quad (1.7)$$

where  $D_+$  and  $\eta_+$  are the positron diffusivity and mobility respectively [6].

### 1.2.2 Moderation

As stated previously, positrons incident on a surface with high kinetic energy are capable of implanting into the material and thermalizing. The average distance diffusing

positrons reach is known as the diffusion length,  $L^+$ . If the incident positrons come to thermal energies within this distance from the surface, they have a chance to diffuse back to the surface. At the surface, it is possible for a few scenarios to occur. One involves the positron falling into a surface potential trap where it will eventually annihilate. Another has the positron pick up an electron, where it can leave the surface as a positronium atom, the atomic bound state of positrons and electrons. One final possibility is to leave the surface as a free positron. In this case, the positron leaves the surface with a kinetic energy which is equal to the positron work function of the material which the target is comprised of, as long as this work function is negative. This probability of this slow positron emission increases as the positron work function of the material becomes more negative [6].

To maximize the number of positrons which are emitted, the number of non-equilibrium defects within the crystal structure, which act as traps for diffusing positrons, must be minimized. To remove these trapping sites, metallic moderators can be annealed *in situ* to approximately  $0.8T_m$  in a good vacuum, where  $T_m$  is the melting point temperature of the material which the moderator is composed. This also cleans the moderator's surface [6].

The emission of slow positrons leads to the idea of moderation efficiency. One definition of moderation efficiency is the rate of mono-energetic positrons reaching a target divided by the total activity of the positron source, although there is an additional definition which replaces the term of the total activity by the rate of fast positrons incident on the moderator [6], we prefer the former definition.

### 1.2.3 Annihilation

Once a positron encounters normal matter, it will eventually annihilate with an electron following a lifetime that is essentially inversely proportional to the local electron

density [3]. Annihilation is a relativistic process where the masses of the two particles are converted into electromagnetic radiation, photons. The form of the annihilation can be determined by invariance properties of quantum electrodynamics. It is possible to have a single photon annihilation event but it requires the presence of a third body to absorb the recoil momentum. This probability of this process to occur is rather negligible [8]. The most probable annihilation process of free positrons occurs when the positron and electron are in a singlet spin state. This process results in the emission of two photons. At low energies, the two annihilation photons are emitted in coincidence with each photon having energy close to 511 keV, the rest mass of both a positron and an electron [3]. The free positron mechanism which involves the emission of three photons is only 0.27% of that of the two photon emission and is only really important in spin correlated bound states, ortho-positronium, where the two gamma process is limited [8]. Higher order process, emission of four or more photons, is expected to be further suppressed [3].

#### **1.2.4 Positronium**

Positronium is the name given to the quasi-stable neutral bound state of a positron and an electron and is given the chemical symbol of Ps. The idea for this hydrogen-like atom was proposed in 1934 by Mohorovičić. The name he gave this bound state, “electrum”, was replaced with the current name of positronium. This atom was eventually discovered in 1951 by Deutsch. It is hydrogen-like, but because its reduced mass equals  $m/2$ , the values of the energy levels is reduced by half from hydrogen, making the ground state energy 6.8eV. It exists in two spin states, a singlet and a triplet, and the particular state has a considerable influence on the energy level structure and the lifetime for self annihilation. The singlet state, where the spin equals 0, is composed of an electron and a positron which are anti-

parallel. This form of positronium is known as para-positronium. The spin 1 triplet state is known as ortho-positronium [3]. Annihilation is governed by the selection rule, which is derived from charge conjugation invariance by Yang in 1949 and Wolfenstein and Ravenhall in 1952. This rule states that the number of photons released,  $n_p$ , depends on the values of the spin and orbital angular momentum  $l$  according the relationship

$$(-1)^{n_p} = (-1)^{l+s} \quad (1.8)$$

For free p-Ps decay must occur by the emission of an even number of photons while for o-Ps, an odd number of photons must be released [6]. The lowest order processes dominate, meaning two or three photons are emitted, although the observation of a five photon decay of ortho-positronium has been reported. The ratio of ortho- to para- positronium has been determined to 3:1 [3]. For para-positronium, the probability for one-photon annihilation is suppressed by the condition that a third body is needed to absorb the excess momentum of the system [6]. In 1946, Pirene, followed by Ore and Powell in 1949, calculated the lowest order contributions to the annihilation rates of p-Ps and o-Ps. The following relationships were determined

$$\Gamma_{2\gamma}(n_{Ps} \ ^1S_0) = \frac{1}{2} \frac{mc^2}{\hbar} \frac{\alpha^5}{n_{Ps}^3} \quad (1.9)$$

and

$$\Gamma_{3\gamma}(n_{Ps} \ ^3S_1) = \frac{2}{9\pi} (\pi^2 - 9) \frac{mc^2}{\hbar} \frac{\alpha^6}{n_{Ps}^3} \quad (1.10)$$

where  $\alpha$  is the fine structure constant and is approximately equal to 1/137.036. For  $n_{Ps} = 1$ , it was determined that  $\Gamma(1^1S_0) \approx 8$  GHz and  $\Gamma(1^3S_1) \approx 7$  MHz, the annihilation rate for p-Ps and

o-Ps respectively. Because the lifetimes are the reciprocal of the rate, it was determined that the lifetime for p-Ps was  $1.25 \times 10^{-10}$  s, or 125 ps, and  $1.4 \times 10^{-7}$  s, or 142 ns, for o-Ps [3].

## 1.3 Positron Sources

### 1.3.1 Radioactive Sources

Positrons can be produced by the  $\beta^+$ -decay of radioactive isotopes. An example of this is the decay of  $^{22}\text{Na}$  by the reaction  $^{22}\text{Na} \rightarrow ^{22}\text{Ne} + \beta^+ + \nu_e + \gamma$ . Because the emission is by  $\beta$ -decay, the positrons are emitted with a broad energy range [2]. Positron decay, or positive beta decay, arises when a proton changes into a neutron with the emission of a positron and a neutrino.



Because the rest mass energy of a neutron is greater than that of a proton, a free proton cannot decay via positron decay in order to conserve energy. However, a proton inside of a nucleus may emit a positron because of the binding energy in the nucleus. Positrons do not exist inside the nucleus before emission; they are created from the conversion of energy to mass in the decay process [9].

### 1.3.2 Pair Production

An alternative approach used to produce positrons is to use high energy gamma rays incident on high-Z elements to create positron-electron pairs [6]. Pair production is one way electromagnetic radiation interacts with matter, which involves the conversion of the photon into the positron-electron pair. A massive atom is required in the vicinity of the interaction to conserve momentum, although the recoil energy imparted to the atom is negligible. The

threshold energy of this process must be 1.022 MeV, the combined rest mass of the electron and positron [10].

One way to use this process is based on a LINAC facility. Electrons accelerated by the LINAC are directed onto a surface and the Bremsstrahlung radiation produced is then used for pair production in high-Z targets such as Ta, W, or Pt. The fast positrons created can then moderate in the target to emitted low energy, eV, positrons. Because LINAC beams are pulsed, this method of production can be used in certain timing experiments [6].

An alternative to the use of a LINAC is the use of other sources of high energy gamma rays. One such reaction that can be utilized is the neutron capture reaction of Cadmium,  $^{113}\text{Cd}(n,\gamma)^{114}\text{Cd}$ , which will produce a continuous beam of positrons. Gamma rays from this reaction sum to the binding energy of the neutron, 9.041MeV. This energy is shared between two or more photons, meaning 2.3 photons are capable of producing a pair production event per neutron absorbed [6].

Nuclear reactors can also be utilized to produce photons of a high enough energy for pair production reactions. In this type of facility, the positron converter/moderator is placed near the core and positrons created are transported out of radiological containment [6].

## ***1.4 Positron Transport***

### **1.4.1 Electrostatic Lenses**

Electrostatic lenses offer the ability to manipulate and focus positrons. It is possible to achieve 100% transmission of particles if the system is optimized [6]. Any electrode which is axially symmetric can act as an electrostatic lens. They not only focus charged particles, but they have the ability to accelerate and decelerate the particles. The lenses

usually consist of nothing more than simple electrodes, which can be nothing more than tubes. Under vacuum conditions, a reasonable requirement of manufacture is that the maximum electric field strength must not exceed 15kV/mm. For positrons, the potentials must be negative; the more negative the potential, the higher the particle is accelerated [11].

### 1.4.2 Magnetic Lenses

As for electrostatic lenses, any axial and symmetric magnetic field can be considered a magnetic lens, although these fields can not accelerate charged particles. In the absence of additional electrostatic lenses, particles exit with the same energy which they enter the lens [11].

While traveling within a magnetic field in the absence of an electric field, charged particles have a simple cyclotron gyration. The frequency of oscillation, the cyclotron frequency is defined as:

$$\omega_c \equiv \frac{|q|B}{m} \quad (1.12)$$

where  $q$  is the charge of the particle,  $B$  is the magnitude of the magnetic field, and  $m$  is the mass of the particle. The solution of the equation of the motion of charge particles in the absence of an electric field, Eq 1.13

$$m \frac{dv}{dt} = q \vec{v} \times \vec{B} \quad (1.13)$$

introduces a new parameter, the Larmor radius, which is defined as

$$r_L = \frac{v_{\perp}}{\omega_c} \quad (1.14)$$

This parameter describes the orbit of the charged particle as it travels within the constant field. The trajectory of a particle within a constant magnetic field and no electric field is generally a helix [12].

## **1.5 Detection and Uses of Positrons**

Annihilation photons can be detected and used to reconstruct the electronic configuration near the site of the annihilation event. Positrons are useful in the study of defects at or near the surfaces of materials [6]. Useful detection techniques include measurement of the lifetime of the positrons in matter and mapping the momentum distribution of electron below surfaces [2], as well as direct imaging of re-emitted positrons from surfaces.

### **1.5.1 Positron Lifetime Spectroscopy**

The lifetime of a positron in condensed matter is a function of the electron density at the site of annihilation. When trapped in an open volume defect, the lifetime of the positron increases compared to the lifetime in a defect free sample because there is a reduction in the electron density in the void. The increased lifetime is related to the size of the defect where the intensity of the event is a measure of the concentration of the defects in the material [2].

The lifetime is obtained by determining the time interval between chosen start signal and the detection of the annihilation photons. Sodium-22, a radioactive positron emitter, emits a 1.28 MeV gamma ray nearly simultaneously with a positron. This gamma ray can be used to trigger the start signal for a lifetime measurement, or by using a microchannel plate, secondary electrons, produced when the positrons strike the surface of the sample, can be detected which can represent a start of the positron lifetime in the sample. Finally, in a beam

system, positrons can be bunched into groups. These groups are equally spaced in time and fields are applied to provide time-focusing. One problem brought about by this technique is backscattered positrons can return to the surface and spread the response time of the detector [6].

The start and stop signals are processed by discriminators and the output pulses trigger a time-to-amplitude converter which acts as the measurement of the lifetime, the amplitude of the output pulse being proportional to the difference between the start and stop signal. This pulse is then sent to a multi-channel analyzer where it can be used to produce a lifetime spectrum [2].

### 1.5.2 Doppler Broadening

Annihilation photons have energies of 511keV, the rest mass energy of the positron and electron, only when both the positron and electron are at rest at the time of annihilation. If there is any excess momentum, the photons will be slightly different from 511keV; therefore, there will be a broadening of the 511keV peak. The change in energy from the rest mass of the electron,  $\Delta E$ , can be determined from the longitudinal component of the momentum,  $p_l$ , by Equation 1.15:

$$\Delta E = \frac{cp_l}{2} \quad (1.15)$$

Because of this, there is a distribution of energies surrounding the annihilation peak, ranging from 511keV -  $\Delta E$  to 511keV +  $\Delta E$ . Modern solid state detectors have the energy resolution to detect this energy shift [5].

The broadening of the distribution about the centroid is usually quantified as the S-parameter, which is often defined as the ratio of the area of the distribution under the central

portion of the peak to that of the total area of the peak. In materials, positrons tend to diffuse to void defects because their energy is lower there. The S-parameter expresses the momentum of the electrons in a material, since the implanted thermalized positrons are low energy at annihilation and therefore contribute little to the total momentum. Core electrons have higher momentum than valence electrons therefore give a broader deviation from the 511keV peak. In voids, there will be more annihilation with outer shell electrons, resulting in a sharper peak [5].

### **1.5.3 Angular Correlation of Annihilation Radiation**

Angular Correlation of Annihilation Radiation, or ACAR, can also be used to examine the electron structure of the bulk of a material and the defects and the momentum resolution is much higher than that of Doppler-broadening. This technique is based on the fact that the two photons are not emitted precisely back-to-back, but have a small angular deviation from exactly  $180^\circ$ . Two-dimensional detection is possible with the use of position-sensitive detectors, such as multi-wire proportional chambers, or Anger cameras. This particular setup filters coincident events of the two detectors and stores the deviation from collinearity in two-dimensional memory. A resolution of  $0.2 \times 0.2$  mrad is achievable.

Defects in the electron structure can be determined by using S parameters like those in Doppler Broadening. The 2D electron momentum distribution is contained in the plots of the coincident events. To obtain plots of just the defects, the information must be normalized for capture of all positrons in defects, which can be done by using an additional positron lifetime measurement [2].

# Chapter 2

## Prototype Design Simulations

### **2.1 Introduction**

The use of positron emitting radioisotopes ( $^{22}\text{Na}$ ) to generate slow positron beams are limited to beam rates of  $10^6$ , maybe as high at  $10^7$  if all conditions were ideal, slow positrons per second with a focus of a few millimeters. The pair production mechanism becomes necessary to produce more intense beams [13]. By placing an appropriate target near the core of a nuclear reactor, which produces high energy photons at an extraordinary rate, an abundant number of positrons can be produced.

### **2.2 MCNP Simulations**

#### **2.2.1 NCSU PULSTAR Reactor**

North Carolina State University was the first campus in the world to own and operate a nuclear reactor. The PULSTAR Reactor is the fourth reactor to be operated on the site and became fully operational in 1972.

Classified as a swimming pool research reactor, the core is placed inside an open 15,000 gallon tank of water [14]. An aluminum tank acts as the pool liner, which is surrounded by concrete shielding. This tank is filled with clean pure water to act as coolant and moderator [15]. The depth of this pool is 26 feet. The core is composed of 359 kg of Uranium Dioxide, which has an enrichment of 4% of Uranium-235. It has dimensions of 24"x15"x13" inches. There are six beam tubes positioned around the core. Beam tube 6 was

utilized for the prototype positron beam. Since this beam tube had a square cross section with dimensions of 12"x12" inches, the moderator could be increased substantially in size to encompass more of the area. It forms a 37° angle to the northwest face of the reactor core [14]. The layout of the beam ports relative to the core can be seen in Fig.2.1.

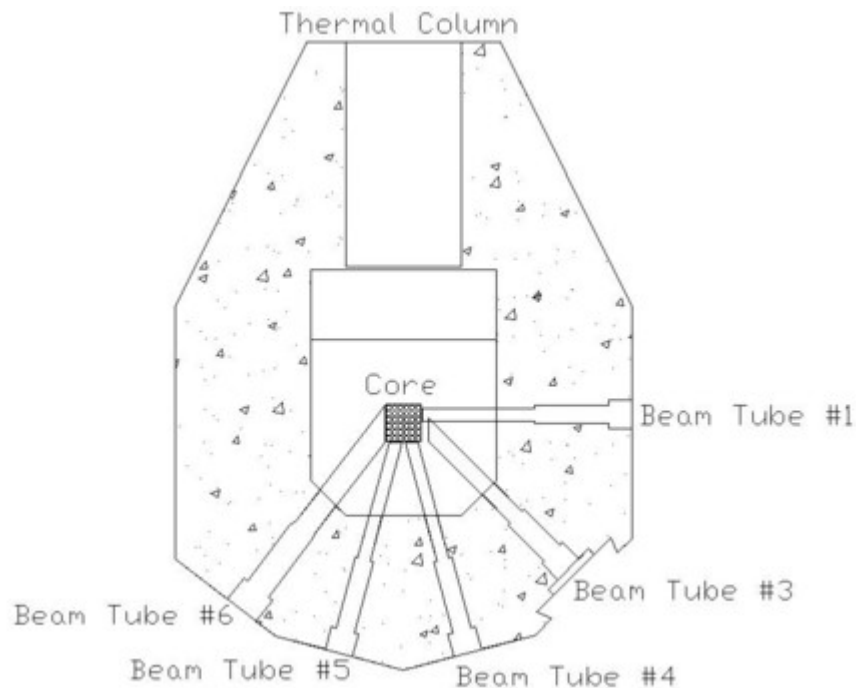


**Fig. 2.1.** Schematic of reactor with biological shield and beam ports<sup>1</sup>

## 2.2.2 MCNP Simulations

The computer program MCNP, Monte Carlo N-Particle code, was used to calculate the flux produced by the reactor. MCNP is a Monte Carlo code capable of continuous energy, time-dependent and coupled neutron/photon/electron transport calculations. To utilize the code, the user must create an input file which defines the geometry of the problem, the materials used in the problem, the definition of the source, and the type of information to be calculated [16].

<sup>1</sup> Courtesy of Mr. Andrew T. Cook, North Carolina State University Nuclear Reactor Program

The Monte Carlo method calculates answers by simulating individual particles and recording the desired characteristic of their behavior. Because the history of the particle is simulated, the actual transport equations do not need to be solved. The program follows many particles from the source throughout the particles lifetime in the geometry, where they are transported between events, collisions for example. Numbers are randomly selected, between 1 and 0, to determine if an interaction were to take place and the type, based on the physics and transport involved [16].

Initial simulations were performed to calculate the photon flux in beam port 6. A model of the core was constructed to match the current geometry of the PULSTAR Reactor; the model utilized can be seen in Fig.2.2.<sup>2</sup>

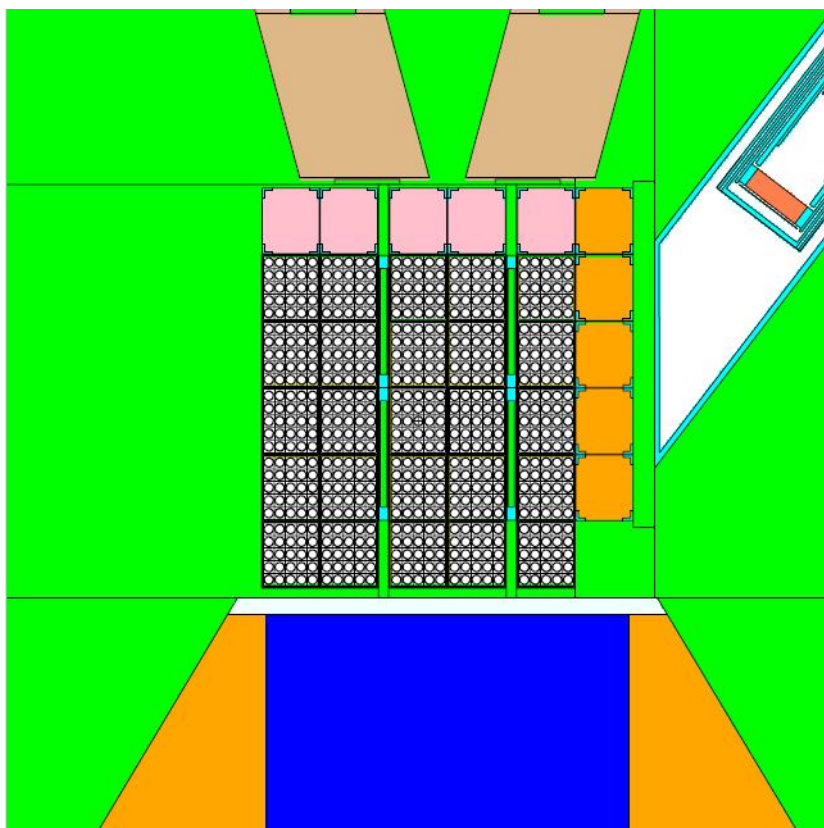


**Fig. 2.2.** Simulation model of PULSTAR reactor core

---

<sup>2</sup> The majority of the MCNP work was performed by Dr. Jianwei Chen while at the Nuclear Reactor Program at North Carolina State University.

Beryllium reflectors are placed in front of the core and graphite reflectors separate the core from the face of beam port 6. The simulated photon flux across beam port 6 is displayed in Fig.2.3.

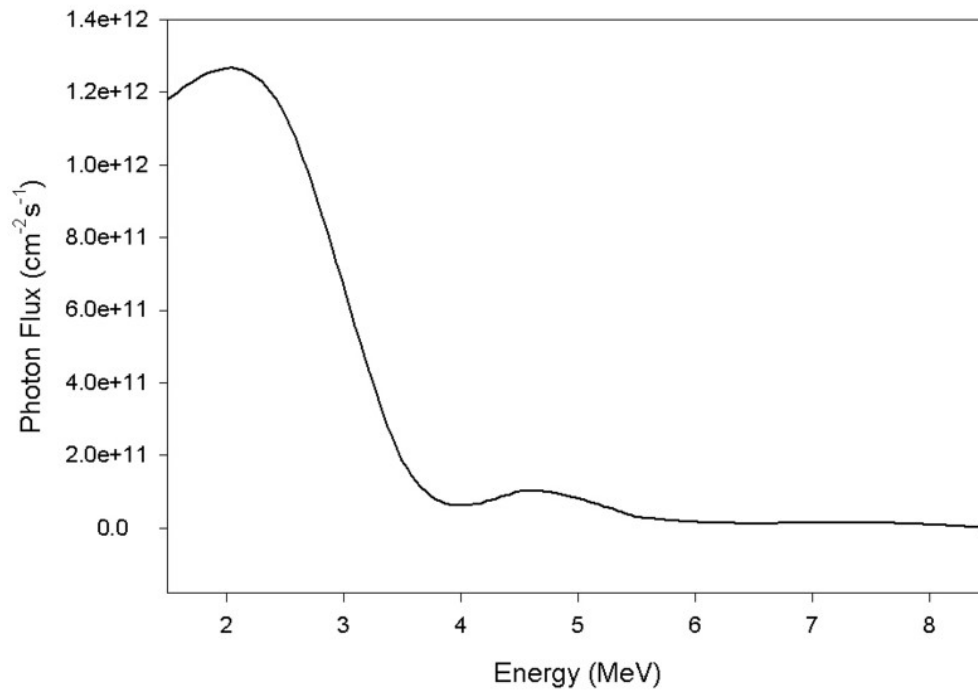


**Fig. 2.3.** Calculated photon flux across beam port 6

The total calculated flux, limited to energies capable of producing a pair production interaction, across beam port 6 is  $2.7 \times 10^{12}$  photons/cm<sup>2</sup>s. MCNP calculates flux using only the prompt gamma rays of the fission reaction, delayed gammas from the fission products are ignored [16]. A correction was utilized so the calculated flux could be increased to compensate for these delayed gamma rays which are ignored.

The photon spectrum could be hardened, i.e. the high energy photon flux increased, and made more intense, by utilizing photon production through thermal neutron capture reactions in a material with a high neutron absorption cross section. To determine the optimum material, a list of the prompt gamma rays emitted by an element was obtained [17].

The elements were sorted by the product of their cross section for the emission of a particular energy gamma ray and the intensity of the emission. The two most favorable elements were found to be Cadmium and Gadolinium. Cadmium was chosen over Gadolinium due to the fact that stock material was already available.

Once the material was chosen, an optimum thickness had to be determined. This optimum thickness would produce the highest amounts of high energy photons without the attenuation of photons present. Further MCNP simulations were performed, this time adding differing thicknesses of Cadmium to the beam port. The results of the simulations can be seen below.

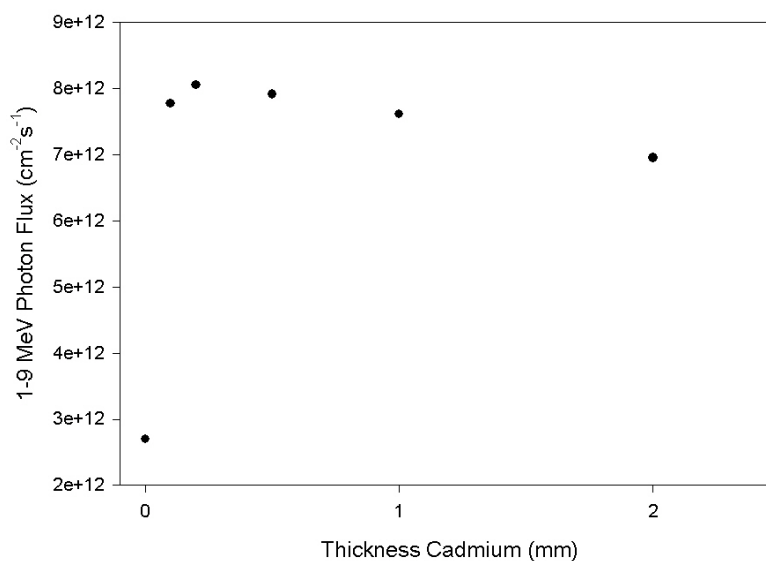


**Fig. 2.4.** Total photon flux vs. cadmium insert thickness

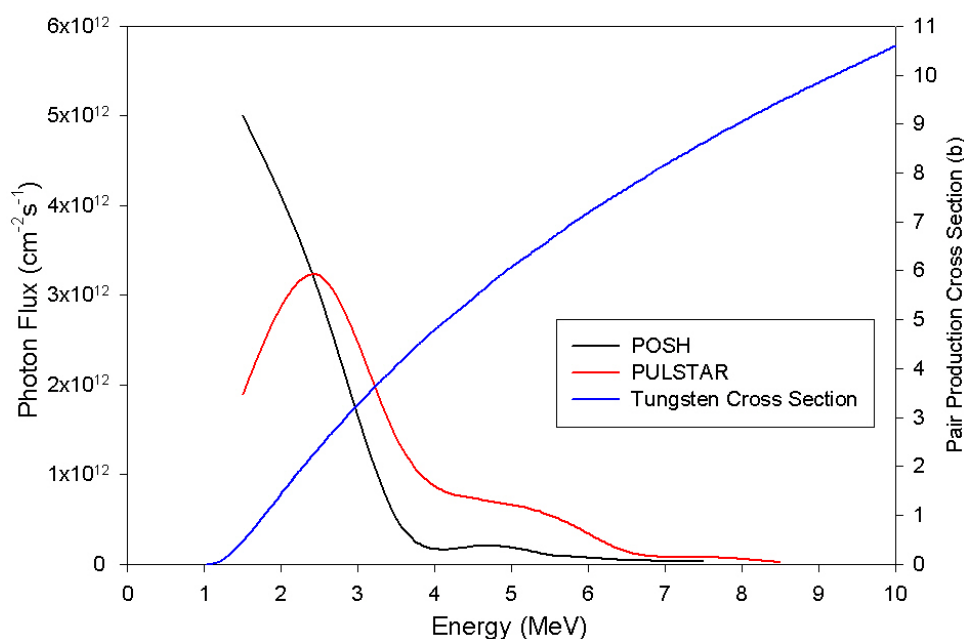
A 0.2 mm sheet is shown to offer the highest total photon flux, which is an enhancement by a factor of 3 over the previous simulation with no cadmium.

Table 2-1 displays the calculated PULSTAR photon flux, broken into energy bins, for beam port 6 with 0.2 mm of Cadmium at the face compared with the photon flux for the POSH positron facility at the Delft Reactor in the Netherlands [18].

**Table 1.** Comparison of energy spectra for POSH and PULSTAR reactors

Gamma Energy	0-1 MeV	1-2 MeV	2-3 MeV	3-4 MeV	4-5 MeV
POSH	---	$5 \times 10^{12}$	$3 \times 10^{12}$	$5 \times 10^{11}$	$2 \times 10^{11}$
PULSTAR	$7.40 \times 10^{12}$	$1.90 \times 10^{12}$	$3.22 \times 10^{12}$	$1.40 \times 10^{12}$	$7.41 \times 10^{11}$
Gamma Energy	5-6 MeV	6-7 MeV	7-8 MeV	8-9 MeV	1-9 MeV
POSH	$1 \times 10^{11}$	$4.5 \times 10^{10}$	$3 \times 10^{10}$	---	---
PULSTAR	$5.50 \times 10^{11}$	$1.41 \times 10^{11}$	$7.91 \times 10^{10}$	$2.03 \times 10^{10}$	$8.05 \times 10^{12}$

In a comparison of the two, the POSH facility has a much greater photon flux in the 1-2 MeV energy bin, although for the higher energy bins, the PULSTAR Reactor has the advantage. The true extent of this advantage can be seen if one plots the photon flux with the cross section for pair production of tungsten [19], as seen in Fig.2.5 below.



**Fig. 2.5.** Photon flux in 1MeV energy bins of the POSH and PULSTAR reactors with the pair production cross section for tungsten

What this figure displays is that the PULSTAR Reactor with 0.2 mm of Cadmium produces more gamma rays that interact with a higher pair production cross section; therefore there is a higher probability for pair production events to occur.

### 2.2.3 Estimation of Beam Rate

Now that the flux has been calculated in beam port 6, it is possible to estimate the positron beam rate that can be produced. This can be done using Equation 2.1 below.

$$R(e^+/s) = \left[ \sum_{i=1}^7 \Phi_i x(f_{int})_i x(f_{pair})_i x(\epsilon_{mod})_i \right] Area_{mod} \quad (2.1)$$

In this equation,  $\Phi$  is the gamma-ray flux in a particular energy bin,  $f_{int}$  is the fraction of gamma rays which cross the moderator that actually interact with the moderator [19],  $f_{pair}$  is the fraction of photon interactions that produce a pair production event [24],  $\epsilon_{mod}$  is the moderation efficiency, and  $Area_{mod}$  is the area of the moderator [13]. The estimated slow positron beam rate for the prototype is therefore  $3 \times 10^8$  Hz, using reasonable values [13].

### 2.2.4 MCNP Optimization

Further simulations could be performed to optimize the orientation of the core to produce the maximum photon flux. It has already been demonstrated that the addition of a 0.2mm layer of cadmium can increase the total 1-9 MeV photon flux by a factor of 3. Previous simulations utilized an input geometry which matched the current configuration of the current PULSTAR Reactor core. The first core optimization attempt was to remove the Graphite reflectors and replace them with Beryllium reflectors, so now Beryllium would separate the core from the beam port, as seen in Fig.2.6. It should be noted that for core optimization simulations, no cadmium was placed in the beam tube. All enhancements mentioned are related to the original calculated total photon flux of  $2.70 \times 10^{12} \text{ cm}^{-2}\text{s}^{-1}$ .

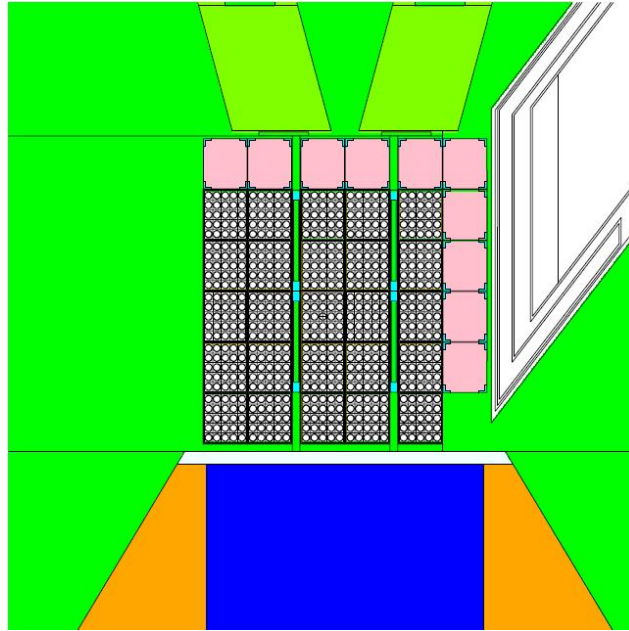


**Fig. 2.6.** Simulation with beryllium reflectors replacing graphite reflectors

The addition of the Beryllium reflector on the right side of the core increased the total 1-9 MeV flux by a factor of 1.17 over that of the configuration currently in use.

The next simulation reversed the core, meaning the Beryllium reflector was placed on the left of the core and the fuel was placed next to the beam port, as seen in Fig.2.7.

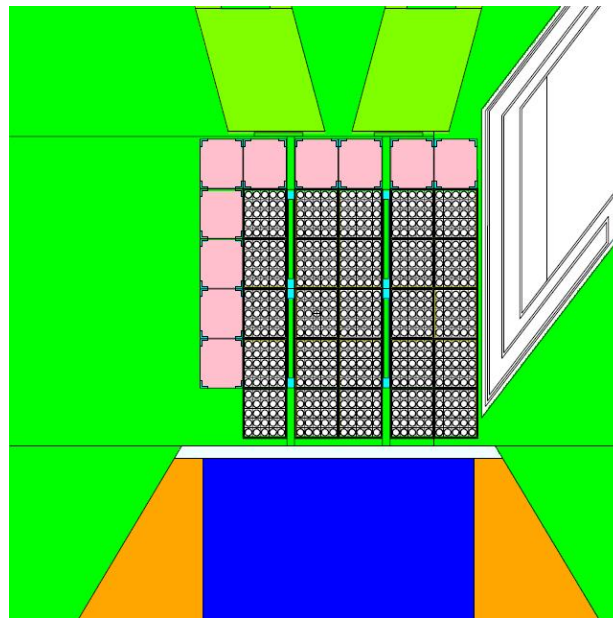


**Fig. 2.7.** Simulation with beryllium reflectors and reversed core orientation

This orientation increased the total flux by a factor of 1.67 over original calculations.

Moving the reflectors to the left side of the core to allow the fuel to be placed next to the beam port was demonstrated to be the optimum core orientation. Simulations could then be performed to again optimize the thickness of the Cadmium layer. A series of simulations were again performed with differing layers of Cadmium, as done previously, this time with the Beryllium reflector on the left. The results of these tests can be seen in Fig.2.8.

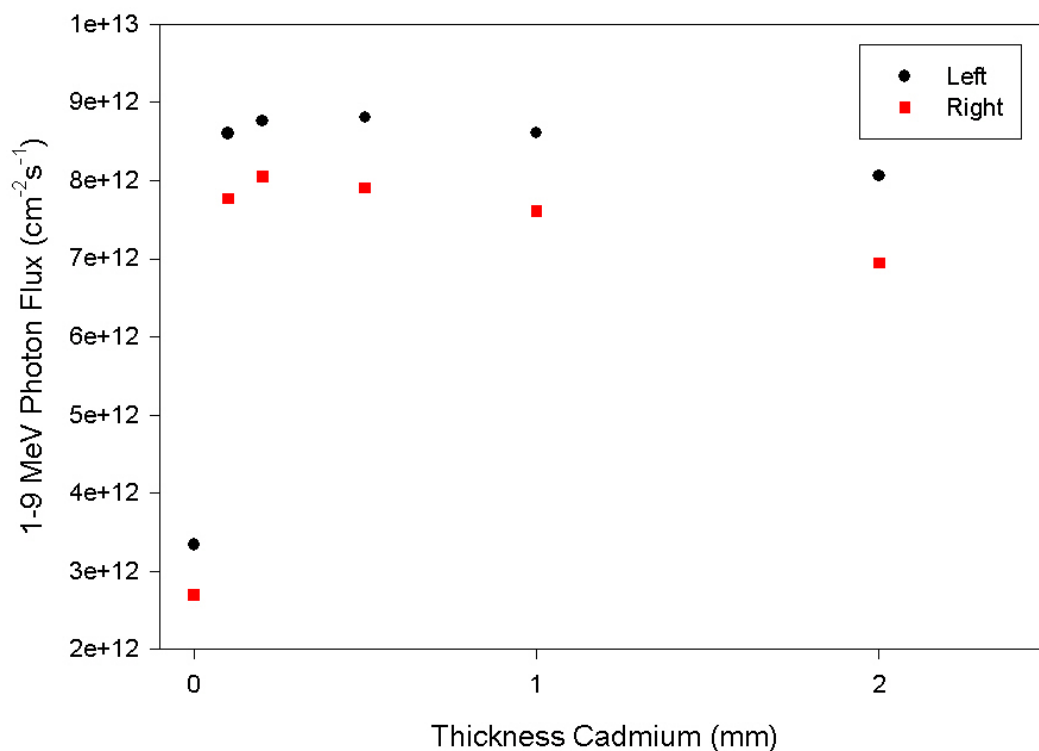


**Fig. 2.8.** Optimization of cadmium thickness with current core configuration and optimize orientation

While there is not a very significant difference between 0.5 mm and 0.2 mm of Cadmium, a 0.5 mm layer offers a slightly higher photon flux. Figure 2-7 also displays a comparison between the effects of the Cadmium for the current configuration of the core against the optimized core design, which offers an increase of 10%.

Further tests were performed to demonstrate how fuel with a higher enrichment would affect the photon flux across beam port 6. This could be done when the core needed to be refueled. All simulations performed so far contained a 4% enrichment of U-235. Tests were performed to calculate the flux across the surface of beam port 6 using fuel with an enrichment of 6%. The first simulation with increased enrichment to be considered had a core orientation of that of the current PULSTAR core, as seen in Fig.2.2 above. This simulation was performed with no Cadmium in the beam. The results of this calculation found that the 1-9 MeV beam port flux increased by 16%. The next simulation replaced the Graphite reflectors with Beryllium reflectors, as seen in Fig.2.6., which offered an enhancement by a factor of 1.16 over initial calculations under a simulation core model. Finally, the core orientation was reversed, i.e. the reflector was placed on the left of the core as seen in Fig.2.7, which increased the flux by a factor of 1.16 over that configuration with a 4% enriched core and a factor of 1.94 over the current core configuration with no cadmium insert.

A final optimization problem that can be calculated is the effect of utilizing Gadolinium rather than Cadmium. A simulation was performed using the current core configuration, with Graphite and Beryllium reflectors as seen in Fig.2.2. A simulation was performed with 0.2 mm of Gadolinium, rather than the Cadmium. The simulated results show that the flux in the beam port was an increase of 7% over the case where 0.2 mm of Cadmium was used.

Upon considering all factors related to the optimization of the core configuration and material selection, an enhancement of the gamma-ray flux by a factor of 2 is achievable while maintaining the power level at 1 MW.

### 2.3 SIMION Simulations

The slow positron beam optics are optimized to collect and transport slow positrons produced near the core out of the beam port, through the biological shield. As a starting point for the design, the example of the Delft positron reactor beam was imitated [18], a long magnetic solenoid lens fed by four electrostatic collection lenses.

The computer program SIMION, which models ion transport through electrostatic and magnetic fields, was used to determine operating voltages to be applied electrostatic lenses. Both the electrostatic lenses and magnetic field were modeled to see the effectiveness of the lens design on the efficiency of ion transport. Three models were produced; one for lenses based on the original Delft design at a one-third scale, one design which replaced the third tapered lens of the Delft design with a straight tube and a final collinear tubular design of the beam.

SIMION allows the user to define the geometry and potential of electrodes and magnetic poles by using potential arrays. The potential for all space within the solution volume can be determined by solving the Laplace equation with the electrodes acting as boundary conditions. The relevant equations are given below:

$$\nabla^2 V = \nabla \cdot \nabla V = 0 \quad (2.2)$$

$$\nabla V = \left( \frac{dV}{dx} \right)_i + \left( \frac{dV}{dy} \right)_j + \left( \frac{dV}{dz} \right)_k = -E \quad (2.3)$$

$$\nabla^2 V = \nabla \cdot E = \frac{dE_x}{dx} + \frac{dE_y}{dy} + \frac{dE_z}{dz} = 0 \quad (2.4)$$

By using Laplace's equation, SIMION is limited to assuming that there is no charge volume density, i.e. there is no space charge. To solve the equation, SIMION uses the finite

difference technique of over-relaxation. This method involves using the nearest neighbor points to obtain new estimates of each point. Once all the points are estimated using this method, additional iterations can be performed which alters the estimates of the previous iteration. When the changes between iterations are small, the potential array is then ready for use in solutions [20].

It is important to note that SIMION is not programmed to trace the field lines of magnetic fields. Magnetic fields are normally thought of in terms of, and measured in, gradients and flux, as opposed to potentials. Magnetic potentials must be defined for SIMION to refine to evaluate a problem [20]. The solenoid to be used was originally designed to be 5 inches in diameter and produce a 100 G magnetic field. To simulate the gradient emanating from the outlets of the solenoid, a shaped pole had to be used. This pole consisted of a flat grid with a parabola at the center to shape the field. This modified pole tried to emulate a field that diminished to 10% of its total value at one radius outside the mouth of the solenoid and 90% of the total field at one radius within the solenoid. A trial and error approach was used to determine the shape of the parabola to produce a field that best matched the given criteria. The diameters of the two poles, located at the front and rear of the beam, were large enough, a significant portion of the length of the beam tube, to ensure that the field between the defined poles would be a constant 100 G field.

For an accurate model of the optical properties of the beam, the phase space of the emitted positrons needed to be determined. The phase space is related to the perpendicular energy of the positrons, perpendicular to the beam axis. With higher perpendicular energy, the positrons will have a greater chance to collide with the lenses of the beam rather be focused into the solenoid. A SIMION model was constructed of a single moderator tube with

the repelling plate and extraction grid, as seen in Fig.2.9. The moderator was set as a ground and the bias plate and extraction grid set to a positive and negative voltage, respectfully. The voltages on these two extraction plates could be optimized to find the highest emission of positrons with the lowest perpendicular energy. The voltages of +/- 40V, +/- 10V and +/- 80V were examined. Positrons were emitted at five equally spaced points from the inner walls of the moderator tube with an initial kinetic energy of 3 eV, the positron work function for tungsten, in a fan of angles ranging from  $-180^{\circ}$  to  $+180^{\circ}$ . This assumption isn't completely accurate for certain materials. Murray and Mills confirmed that thermalized positrons are emitted from a single crystal surface essentially normal to the emission surface. It has also been determined experimentally that angular spread of emitted slow positrons from single crystals is approximately equal to  $2[kT/(-\phi_+)]^{1/2}$ . This relationship shows that the angular spread is dependent on the temperature of the surface [6]. But, the polycrystalline nature of the tungsten tubes gives a much broader angular spread than the single crystal results, justifying the broad fan of angles. Figure 2.9 displays the model used including positron tracks from the five emission points.

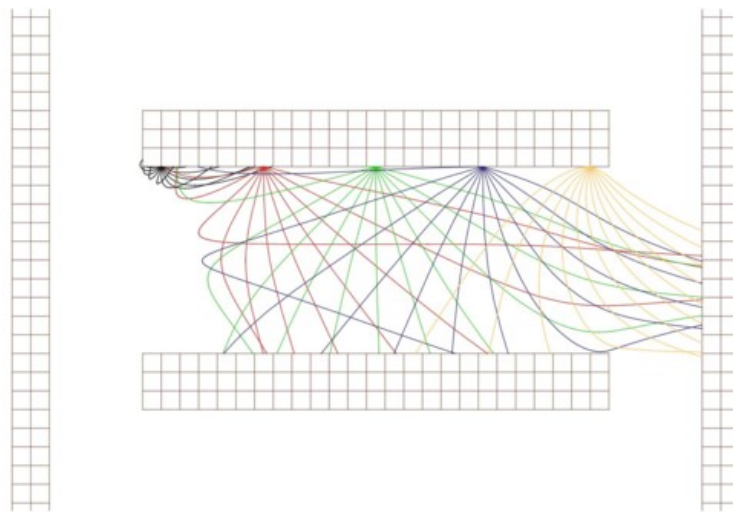


**Fig. 2.9.** Simulation of moderator tube with five equally spaced emission points

The extraction grid is placed on the right and repelling plate on the left.

To utilize this model, SIMION recorded the x and y component energies and the total energy of the positrons when they were stopped by the surface which represents the extraction grid. The output data was examined and those particles which did not have a total kinetic energy of at least that of the extraction grid, which has 40 V of acceleration, were thrown out because those particles would have collided with the simulated tungsten moderator and would have not escaped the moderator. *The concept of positron bouncing was not considered when performing this simulation.* With the x and y component energy data of the remaining particles, the perpendicular energy was calculated using the following equation [21]:

$$E_{\perp} = E_{Total} \left( \sin \left( \tan^{-1} \left( \frac{v_y}{v_x} \right) \right) \right)^2 \quad (2.5)$$

In this equation,  $E_{Total}$  was the emission energy of the positrons, 3 eV, added to the withdrawing potential of the grid (either -10V, -40V, or -80V). Histograms were produced to display the number of particles with a given perpendicular energy. The following figure displays the results for a test with voltages of +/- 40V.

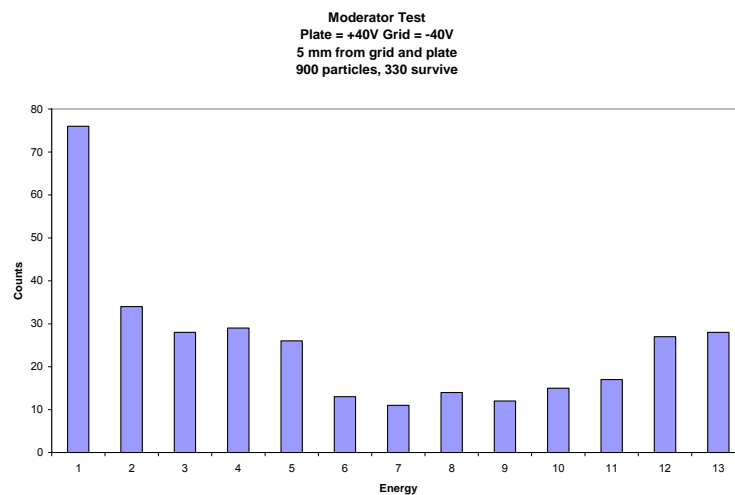


**Fig. 2.10.** Histogram of possible perpendicular energy with plate potential of +40V and grid potential of -40V

Slightly more than one third of the particles, 330, escape to the moderator to strike the grid. The maximum E-perp was 13 eV. Figure 2.10 shows the results of the test with voltages of +/- 10V.

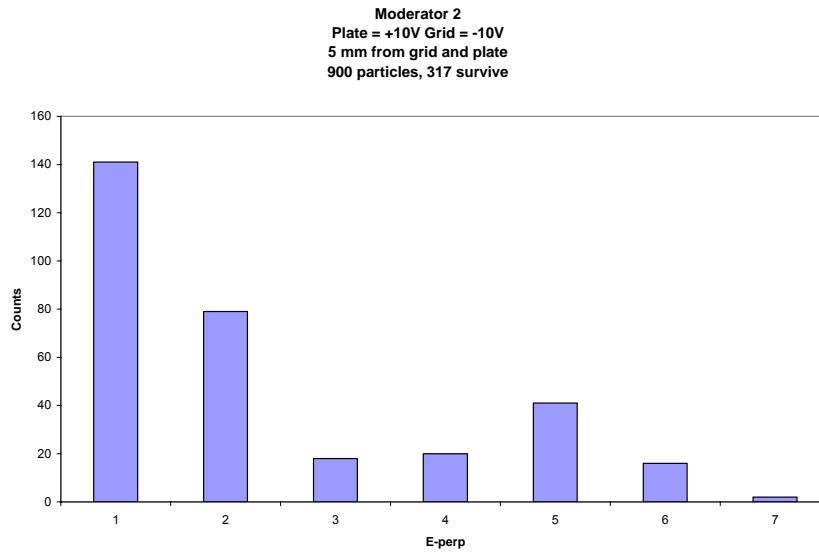


**Fig. 2.11.** Histogram of possible perpendicular energy with plate potential of +10V and grid potential of -10V

The maximum E-perp for this run was 7eV and only a third of the particles, 317, survived.

Finally, +/- 80V was tested and the results are summarized below.

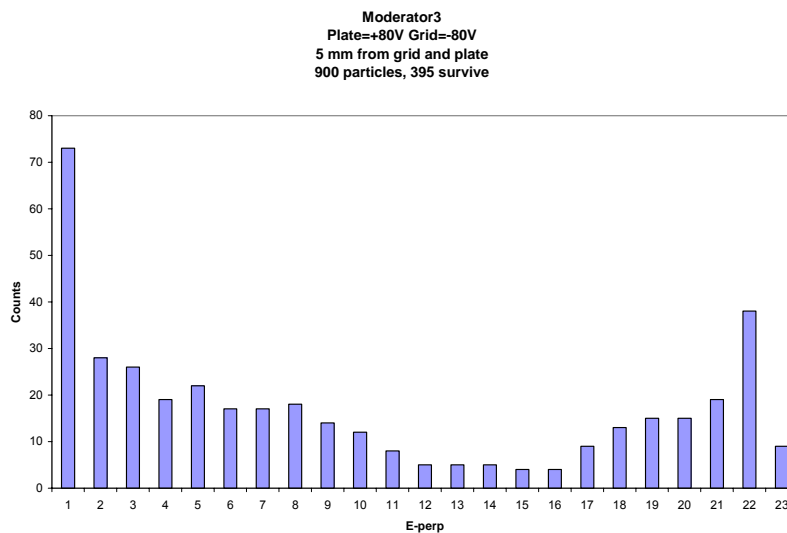


**Fig. 2.12.** Histogram of possible perpendicular energy with plate potential of +80V and grid potential of -80V

In this case, the maximum E-perp was 23eV and nearly 40% survive. After looking at the calculated data, the +/- 40V option optimized the yield and initial energy width of the beam and was therefore thought to be the best choice for the voltages for the plate and grid.

There was now enough data to produce a model of the beam which could reasonably model the reality of slow positron emission. The simulation above resulted in a reasonable assumption for a perpendicular energy value of 13eV, instead of an intuitively guessed value. This allowed the positrons to be randomly emitted from the grid plane, which then represents the moderator, rather than a full model of the moderator. The positrons were emitted with an initial energy of 13eV in a fan of angles from  $+90^\circ$  to  $-90^\circ$ . For the positrons to contain initial emission energies of 3eV relative to ground, the emission plate from which the particles were emitted was given a potential of -10V. Particles were emitted from three approximately equally spaced spots from the axis of the emission plate and towards the extraction grid with a potential of -40V.

The first test performed, seen in Fig.2.13, was of the original Delft configuration.

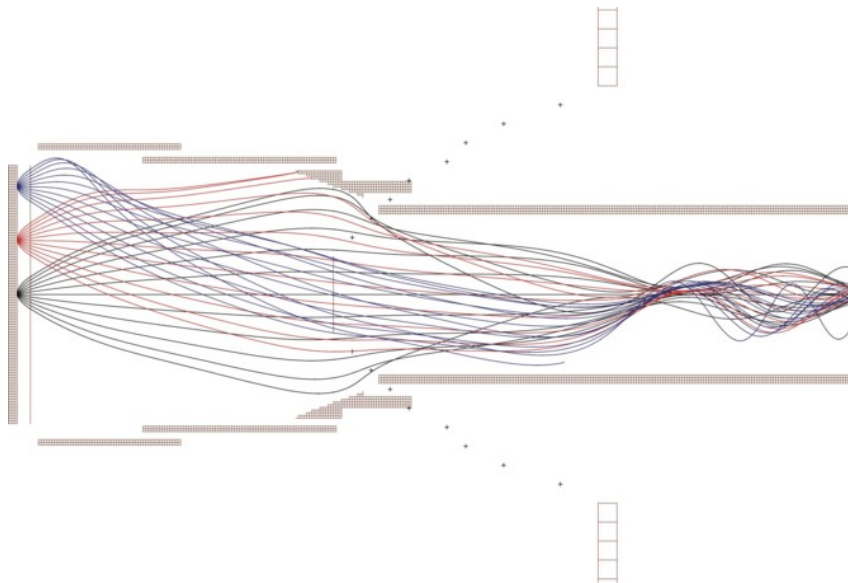


**Fig. 2.13.** Simulation of one-third scale Delft design

Voltages were scaled to one third of their original values. The first lens, relative to the moderator, is set to ground, the second is set to -200V, the third to -133V and the fourth to -1000V (this last voltage sets the transport energy through the long solenoid). As seen in the figure, some of the higher energy and high angle positrons further away from the axial position strike the lenses. Also, some of the high angle positrons, i.e. high perpendicular energy, emitted from the axial position contain very sharp turns in their trajectory.

The lens voltages were altered to increase the number of positrons that survive transport through the electrostatic lenses. Figure 2.14 displays the first attempt to improve the survival of the positrons.

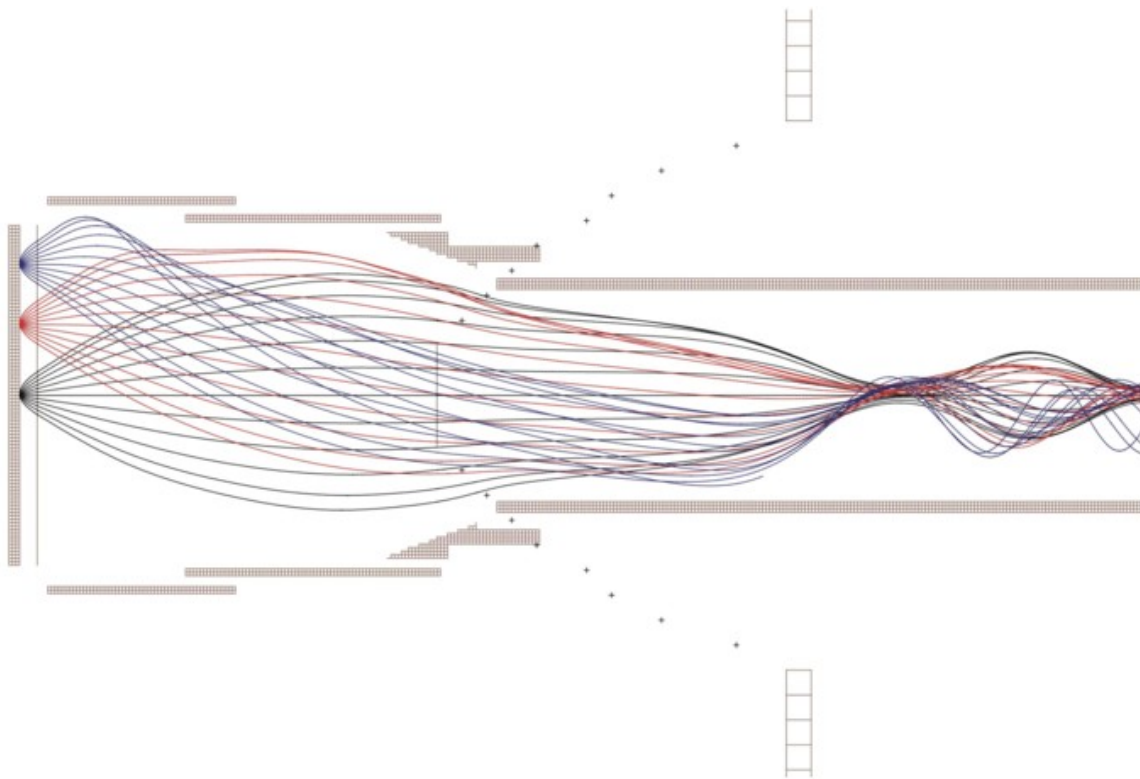


**Fig. 2.14.** Simulation with Delft lens design with altered lens voltages

The voltage of the first lens was again set to ground, the second lens was -100V, the third -300V and finally the fourth was set to -1000V. In this particular case, no particle seems to

hit any of the lenses, although one does stop for reasons unknown. Further adjustments to the voltages were attempted and the results are displayed in the figure below.

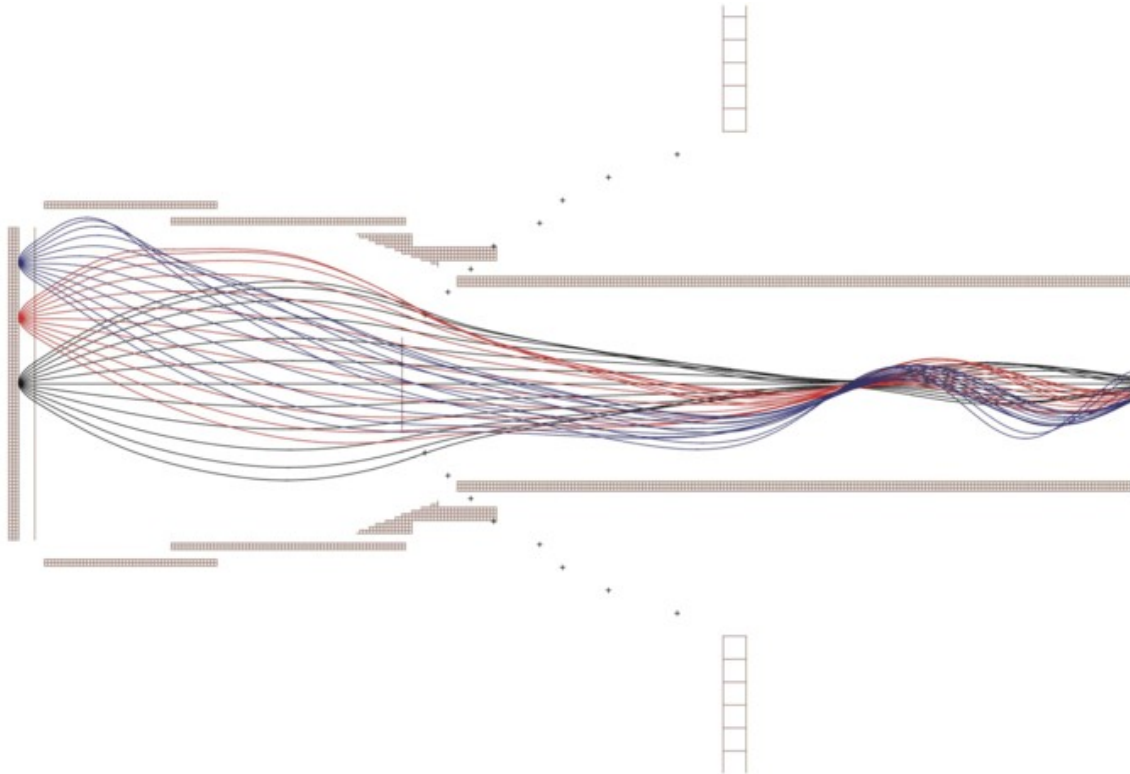


**Fig. 2.15.** Simulation with transport lens 4 increased to -2000V and the first lens set to -5V

This run had voltage of -5V, -100V, -300V and -2000V, for lenses one through four. The -2000V adjustment helps to draw positrons from the focusing lenses into the mouth of the solenoid. All of the particles are again able to make it through the solenoid.

Attention then shifted to simulations which replaced the third tapered lens with that of a straight tube of the same inner diameter and the same overlap of the second lens was maintained. After continued runs, an approximate one to four ratio of voltages for lenses two through four demonstrated a successful configuration for lens voltages. The results for this run can be seen below.

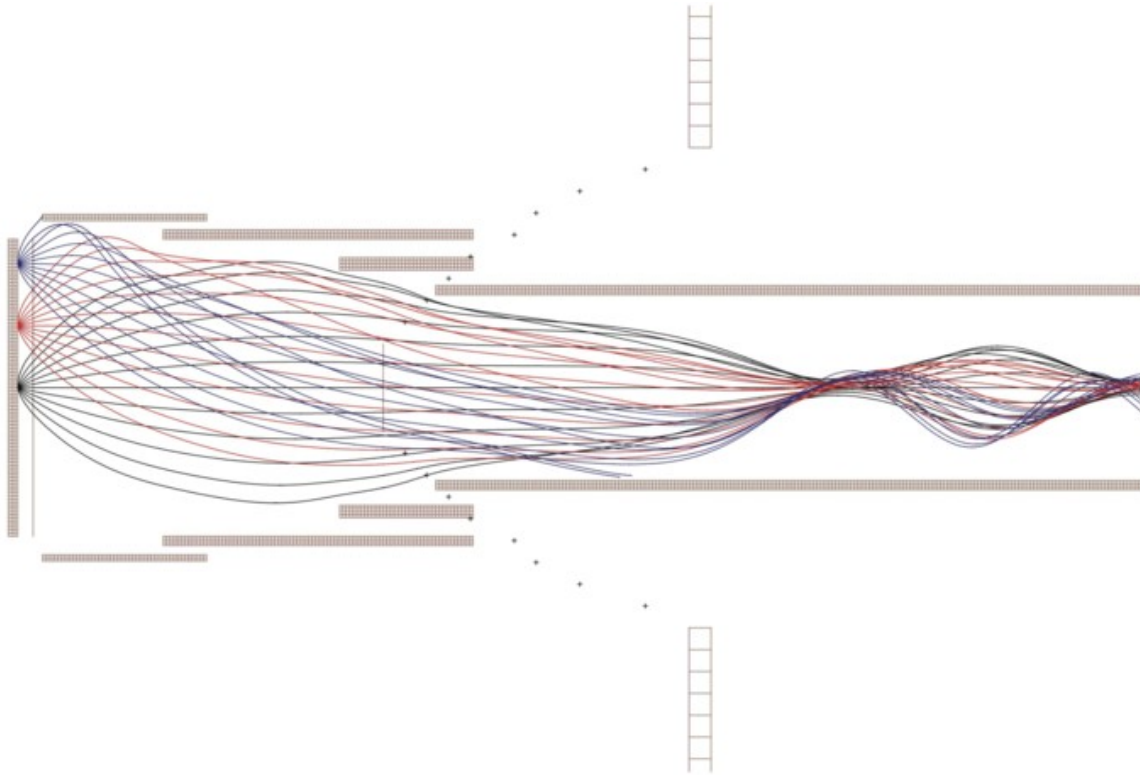


**Fig. 2.16.** Simulation with voltages on adjacent lenses in approximate 1:3 ratio

The working voltages decided upon for use in the prototype were -200V for lens two, -700V for lens three and -2000V for lens four. Focusing seemed to stay the same for the beam as long as this 1:3 ratio was maintained for those lenses. Altering lens one seemed to have the most influence on how well the beam worked, the upper limit for successful transmission of all modeled positrons being approximately -20V.

Next, simulations were run to produce a series of runs which have a range of perpendicular energies. The same voltages were used on each lens for each test. To simulate the range of perpendicular energies, the initial energy was altered from 8eV to 25eV but the potential placed on the emission plate was altered accordingly to maintain a positron emission of 3eV relative to ground. The results of these simulations are presented in Fig.2.17.

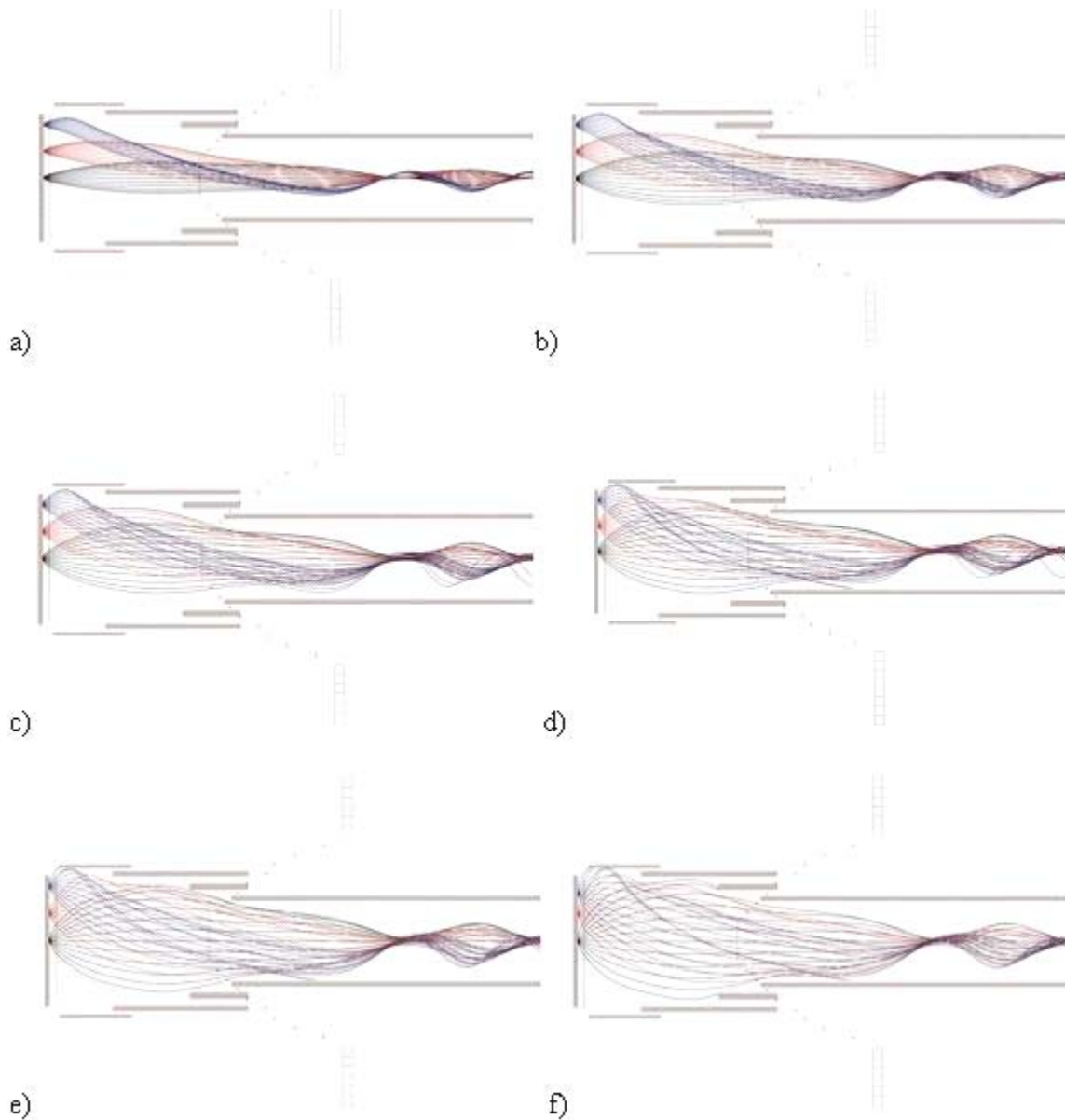


**Fig. 2.17.** Series of simulation with altering emission energies; a) 3eV, b) 8eV, c) 13eV, d) 20eV, e) 25eV, and f) 30eV

Problems do not really begin to be encountered until a perpendicular energy of 20eV. It isn't until the positrons obtain a perpendicular energy of 30, as seen in Figure 2-16 f, transmission problems begin to arise for positrons emitted from each of the three locations. By performing these simulations over a broad range of perpendicular energies, it can be seen that

the lens design is robust and will be able to handle positrons with many perpendicular energies.

Further simulations had to be performed once the electrostatic lens design was altered to the tubular design. After further analysis, the final working voltages selected for use in the prototype electrostatic lens system were:

**Table 2.** Working Lens Voltages utilized in prototype beam

Lens 1	-10V
Lens 2	-200V
Lens 3	-700V
Lens 4	-2000V

The results of the simulation of the final lens design are shown in Fig.2.18.

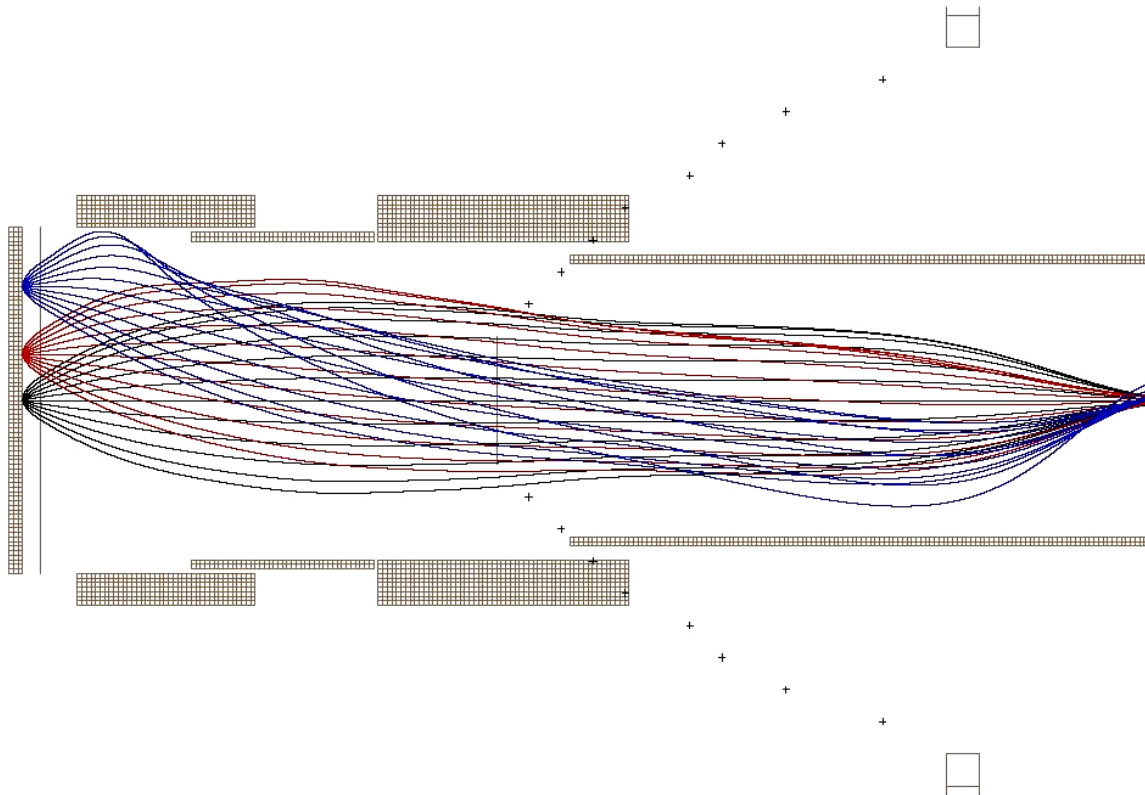


**Fig. 2.18.** Simulation of tubular lens design

Once the positrons are successfully focused into the mouth of the solenoid, they are transported with high efficiency through the beam to the target. The efficiency of the magnetic field transport can be seen in Fig.2.19.

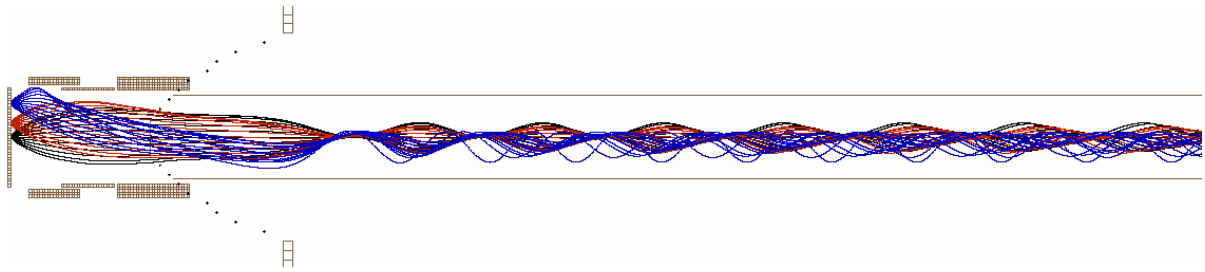


**Fig. 2.19.** Simulation of positron focusing and transport

## Chapter 3

# Construction of Prototype Slow Positron Beam<sup>3</sup>

### 3.1 *Material Selection*

The internal components of the beam were designed with neutron activation in mind. A majority of the components are constructed with 6061 T6 Aluminum, the few exceptions being approximately 50 g of tungsten for the moderator, several grams of ceramic insulators, and a small amount of stainless steel from screws [13]. To increase the number of high energy photons crossing the moderator, a cadmium cap was applied to the end of the beam.

An analysis was performed to determine what the dose rate of the components would be if the beam had to be removed for repair. For calculation, it was assumed that the reactor had been running for a long duration for 42 hours per week. The dose rate was calculated after 60 hours of decay, assuming a problem occurred and the reactor was shut down and allowed to cool for the weekend [22].

For the moderator, the tungsten and titanium foils which surround the moderator are shrouded by a cadmium cap, which is estimated to reduce the thermal neutron flux by a factor of 1000 but leaving the fast flux virtually unchanged. The various isotopes of tungsten and titanium, and for all isotopes examined for the entire beam in additional analysis, are examined to see which reactions are energetically possible with neutrons emitted from the

---

<sup>3</sup> The construction of the prototype positron beam was performed at the laboratories of the Michigan Positron Group at the University of Michigan, Ann Arbor, under the supervision of Prof. David Gidley. Dr. Mark Skalsey headed the project with support from Dr. William Frieze and the rest of the Michigan Positron Group.

nuclear chain reaction. Reactions not possible, weak radiations and isotopes with short half-lives are not considered. The following table summarizes the results for the major radiations.

**Table 3.** Induced Radioactivities in the Converter/Moderator Assembly after 60 hours

Isotope	Half-life	Equilibrium Activity	Major Radiations
$^{187}\text{W}$	23.7 h	29 mCi	$\beta^- \approx 0.54\text{-}1.31$ MeV $\gamma \approx 0.5$ MeV $\approx 30\%$
$^{185}\text{W}$	75.1 d	7.8 mCi	$\beta^-$ 0.44 MeV
$^{46}\text{Sc}$	84 d	3.3 mCi/kg Ti	$\beta^-$ 0.36 MeV $\gamma$ 0.9, 1.1 MeV both 100%
$^{47}\text{Sc}$	3.4d	40 mCi/kg Ti	$\beta^- \approx 0.6$ MeV 32% 0.4 MeV 68% $\gamma$ 0.16 MeV 68%

$$\left( \Phi_n^{th} = 1 \times 10^{10} \text{ n/cm}^2 - \text{s}, \Phi_n^{fast} = 5 \times 10^{11} \text{ n/cm}^2 - \text{s} \right)$$

The tungsten gamma dose after 60 hours of cool down is calculated to be 2.6 mR/hr at 1 meter and 5.8 mR/hr-kg for titanium at the same distance and decay time. The moderator could be safely removed for storage after one weekend of decay [22].

The majority of the beam is comprised of 6061 Aluminum. This alloy is composed of approximately 98% aluminum with the remainder being magnesium, silicon, and other elements. Because the flux falls with distance away from the core, the dose rate at the end furthest from the core is dominated by that of the hot end. Table 2 summarizes the results.

**Table 4.** Maximum Induced Radioactivities in 6061 Al Alloy after 60 hours

Isotope	Half-life	Equilibrium Activity	Major Radiations
$^{24}\text{Na}$ (from Al)	15.0 h	5 $\mu\text{Ci/kg}$	$\beta^-$ 1.4 MeV $\gamma$ 2.75 and 1.4 MeV 100% each
$^{24}\text{Na}$ (from Mg)	15.0 h	50 $\mu\text{Ci/kg}$	$\beta^-$ 1.4 MeV $\gamma$ 2.75 and 1.4 MeV 100% each
$^{64}\text{Cu}$	12.7 h	74 mCi/kg	$\beta^-$ 0.6 MeV 40% $\beta^+$ 0.7 MeV 19% $\gamma$ 1.34 MeV 0.6% 0.5 MeV 38% ( $e^+e^-$ )
$^{51}\text{Cr}$	27.7 d	520 mCi/kg	$\gamma$ 0.32 MeV 10%

$$\left( \Phi_n^{th} = 1 \times 10^{12} \text{ n/cm}^2 - \text{s}, \Phi_n^{fast} = 5 \times 10^{11} \text{ n/cm}^2 - \text{s} \right)$$

The dose rate at 1 meter is calculated to be 17.6 mR/hr-kg, which would allow for safe removal after one weekend [22].

### 3.2 The Moderator/Converter Assembly

The moderator/converter assembly converts the high energy photons into positrons, most importantly, slow positrons. As stated previously, positrons produced through pair production usually have high energy.

There are numerous materials which can be used to moderate positrons. One desirable characteristic of the moderator/converter based on pair production is that it has a high atomic number. This is because the cross section of this photon interaction increases with the square of the atomic number of the target, i.e.  $Z^2$  [23]. This is because, as stated previously, the interaction requires the presence of a massive nucleus to conserve momentum [10]. Figure 3.1 [24] demonstrates the probability of the occurrence of a pair production event against the energy of an incident photon for various materials. As can be seen, the probability increases for lower incident energies as  $Z$ , the atomic number, increases.

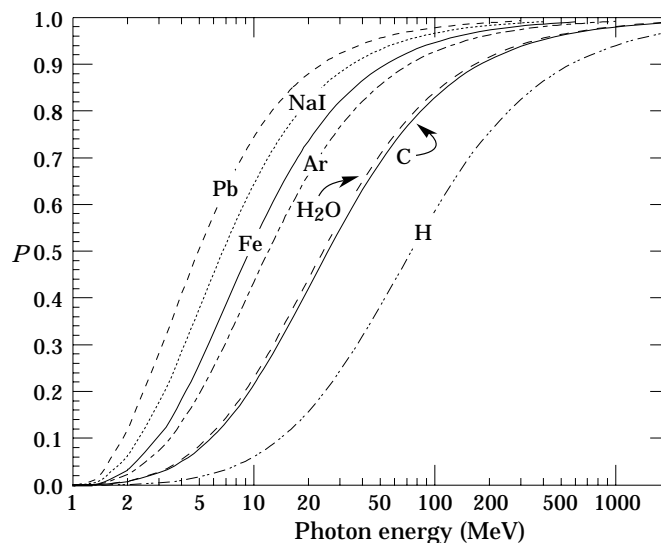


**Fig. 3.1.** Relative probability of occurrence of pair production event vs. incident photon energy for various elements

Another factor that must be taken into consideration is the positron work function of the material. As mentioned in the previous chapter, if thermalized positrons can reach the surface of a material, they can possibly be ejected from the surface with energy equal to the positron work function, as long as this value is negative. The probability for this event to occur increases as the positron work function becomes more negative [6].

After considering these two desired characteristics, Tungsten was chosen as the moderator/converter material. Having an atomic number of 74, there should be a high probability for pair production to occur. It also has a positron work function of approximately -3 eV, a very high value compared to other materials. The use of tungsten has other advantages as well. Well annealed tungsten can obtain moderation efficiencies as high as  $10^{-3}$ . It can also be annealed and then transported through air without significant degradation of the moderator [6].

The geometry of the moderator was adopted from the original moderator/converter constructed at the Delft reactor in the Netherlands. The prototype moderator consisted of 55 Tungsten tubes in a semi-hexagonal array, made from commercial tungsten foil. The dimensions of each tube were approximately 1 cm in diameter and 2.5 cm long. The walls of the tungsten tubes were approximately 0.05 mm thick. Ordinarily, bulk tungsten is brittle but thin foils, wires and ribbons are ductile and elastic before annealing, a fact which will be utilized later in the final construction of the moderator. To obtain the desired diameter, the foils were inelastically deformed around a 0.5 cm diameter rod.

Compression holds the tungsten tubes in the semi-hexagonal array. A one inch aluminum tube, with an outer diameter of 3.75 inches and an inner diameter of three inches, is used as a moderator/converter holder. The tungsten tubes are loosely arranged inside of

the holder. Six titanium strips are bent to approximately  $60^\circ$  and are placed around the array. Six small aluminum blocks are placed between the titanium and the inner surface of the aluminum tube. The compression supplied by these aluminum blocks and the natural elasticity of the tungsten is utilized to hold the array together. The tubes are arranged so that the tubes are parallel to the axis of the beam [13]. Figure 3.2 displays a mockup of the finalized moderator design.



**Fig. 3.2.** Mockup of moderator/converter array

A repeller plate was placed behind the moderator/converter array which would have a positive potential placed upon it to push positrons towards the front of the array. An extraction grid, with a negative potential, was placed in front of the array to remove emitted positrons from the moderator and propel them into the focusing portion of the beam. If the voltages on these two electrodes were reversed, the beam was effectively cut off, i.e. slow positrons could not reach the focusing portion of the beam. This feature was used to determine the true number of slow positrons emitted during measurement studies.

Annealing studies were performed on the tungsten tubes at the University of Michigan by Dr. Mark Skalsey and Steve Chapman using a miniature beam. An Antimony-124, Sb-124, gamma-ray source was used to produce the positrons using pair production.

The source was placed behind the moderator and beam. Initially the beam on and beam off rates were statistically identical; beam on meaning that the lens potentials are configured in a way that the slow positrons are pulled from the moderator to be detected and where beam off reverses the configuration. This lack of slow positrons was understood because the tungsten tubes had not been annealed. Heating tests began with a temperature of 200°C and then to 300°C but there was no sign of slow positrons for either case. Next, the tubes were heated to 600°C and finally 1000°C. A slow positron signal was recognizable above background with heating up to 1000°C, although the results could not be reproduced one month later. Further heating was performed with a 2.5 kW RF induction heater with an operating coil in a vacuum system. This allowed heating to temperatures as high as 2300°C. Groups of tubes were bound together then placed inside the RF coil on a ceramic table and heated at a pressure of  $10^{-6}$  torr. After heating, the tubes were stored in vacuum until all annealing was completed and the test moderator was ready to be assembled. After annealing, the tubes seemed brittle and there may have been some localized melting, where the tubes stuck together. Testing showed the final annealing had an efficiency eight times higher than heating at 1000°C. Before construction of the final prototype moderator/converter array, the tubes were reheated to remove any surface contamination that may have been built up from the completion of the pre-prototype tests and the final prototype [13].

### **3.3 Beam Design**

The prototype positron beam was designed to slide into a 6 inch schedule 40 aluminum pipe. The beam was designed so it could fit into any of the available beam ports of the NCSU PULSTAR Reactor. Figure 3.3 displays the general design of the beam placed inside a beam port.

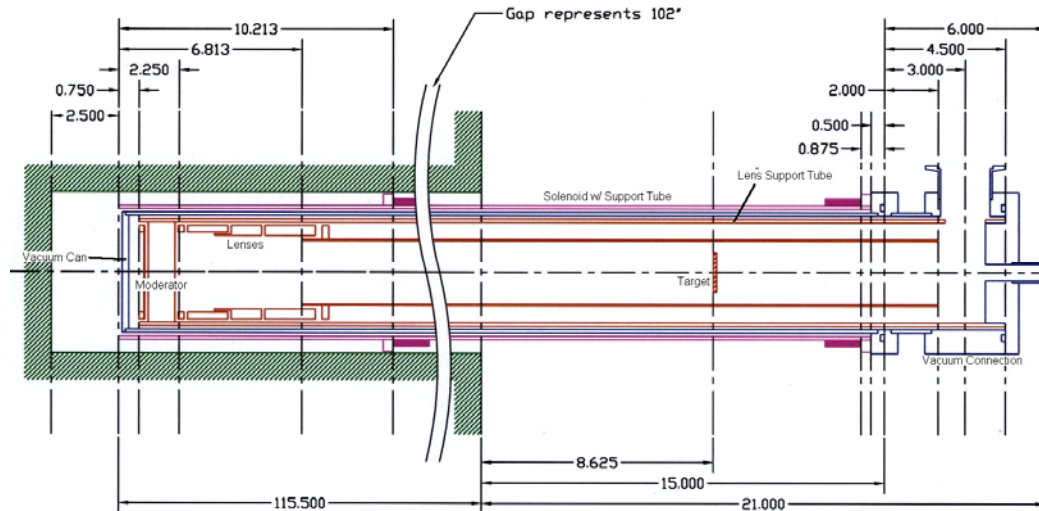


**Fig. 3.3.** Layout of positron beam in beam port<sup>4</sup>

It consists of concentric aluminum tubes of decreasing diameter, which allows the ability to remove individual components of the beam without the removal of the entire apparatus if an internal problem were to occur. The largest diameter tube has the solenoid wound upon it. All other components slide into this solenoid support tube. The next layer is the vacuum tube and finally a tube is used to support the electrostatic lenses of the beam.

### 3.3.1 Solenoid Design and Construction

The solenoid supplies a uniform axial magnetic field which transports positrons out of the biological shield. Originally, the solenoid was designed to consist of four layers of 14 gauge wire. As the number of layers increases, the power required by the solenoid decreases, therefore cooling can be accomplished by air cooling.

A solenoid can be considered as an arrangement of individual current loops adjacent to each other [11]. Current flowing through a wire gives rise to magnetic fields, which can be calculated using the Biot-Savart Law, which can be seen in Equation 3.1.

<sup>4</sup> Courtesy of Dr. William Frieze, University of Michigan

$$d\vec{B} = \frac{\mu_o I d\vec{L} \times \vec{r}}{4\pi r^2} \quad (3.1)$$

where  $\vec{B}$  is the magnetic field,  $\mu_o$  is the permeability of free space,  $d\vec{L}$  is an infinitesimal length of the wire carrying current  $I$ , and  $\vec{r}$  is a unit vector describing the direction to a point a distance of  $r$  away from the conductor [25]. In the case of a current loop,  $\vec{r}$  points in a radial direction towards the axis of the loop and  $d\vec{L}$  would be located on the circumference. The right-hand-rule can be utilized on the cross product,  $I d\vec{L} \times \vec{r}$ , demonstrating the magnetic field is in the axial direction, the orientation of which depends on the direction of the flowing current.

A solenoid support tube was designed to wind the solenoid upon. It was simply an aluminum tube with an outer diameter of 5 inches and approximately 11 feet long, 130 inches in length to be exact. Two end flanges were then welded to the support tube to act as the limits to the length of the solenoid. One flange was positioned at the very end of the aluminum tube. This flange had grooves to enable the start of the solenoid winding to have no kinks. A second flange was located approximately 10 inches from the opposite end of the tube. This 10 inch region of the tube is where the lenses of the beam would be positioned; the stronger magnetic field would not allow the electrostatic focusing of the lenses. The actual solenoid could then have a length of 119.415 inches, or approximately 10 feet. The flanges added to the solenoid support tube had an outer diameter of 5.875 inches. This length, 5.875 inches, is the total diameter of the entire beam and can easily fit inside any of the 6 inch beam ports.

Similarly to the design located at the Delft Reactor, it was decided to utilize 14 gauge anodized aluminum wire in the construction of the solenoid. The use of aluminum wire

eliminates activation problems which would occur if copper wire was used. Also, the aluminum oxide insulation eliminates radiation damage that would occur in typical polymer insulations. Approximately 16000 feet of aluminum wire was ordered, more than enough to wind four solenoid layers. To determine the amount of wire necessary for winding the solenoid, one first needs to know the number of turns which could fit within bounds of the flanges on the solenoid support flange, which would simply be the distance, 10 ft, divided by the diameter of the wire being used, 0.064 inch. This estimates the number of windings to be approximately 1,875 windings. The length of each winding would simply be the circumference of the solenoid, or approximately 16 inches, therefore, the length of wire needed would simply be the product of the length of a winding and the number of windings. By multiplying by the number of layers, one can obtain the total amount of wire necessary. A cart was constructed to suspend and transport the spool of wire and the offer tension to the wire during the winding process. The solenoid support tube was attached to a rotating welding head with the opposite end supported by rollers, as shown in Fig.3.4. A small track was position parallel to the tube, which allowed the wire to be slid parallel the tube. Once the rotating head was turned on, the support tube easily drew wire from the cart and began the winding.



**Fig. 3.4.** Picture of winding setup

After winding a short distance, it was discovered that the solenoid was shorting to the support tube. This was discovered by attaching an ohm meter to the wire and touching the support tube. Current was seen traveling through the support tube. The current traveling in a loop is necessary to produce the magnetic field; therefore, the short removes the ability of the wire to produce the magnetic field. It was believed that the wire contained small fractures in the insulation. The decision was then made to coat the aluminum tube with an aluminum oxide based potting material for electric insulation to eliminate the problem. The support tube was polished to ensure that there were no sharp or rough areas which could cut into the fragile and thin insulation.

After the potting material was applied to the tube, a solenoid layer was successfully wound. Unfortunately, layer to layer shorts, shorts between the layers of the solenoid, were then discovered. Additional insulation, a ceramic fabric composed of aluminum oxide, was wrapped around the first layer of the solenoid, isolating it from the second layer. The second layer of the solenoid was then successfully wound. This layer was again covered in the ceramic fabric and potting material. The thickness of the solenoid was successfully under the limit of 0.875 inches imposed by the solenoid support tube end flanges.

Due to wire lost in winding the solenoid and discovering shorts and the additional thickness added to the solenoid by the insulation, the final solenoid contained only two layers. Two values are important in characterizing the solenoid. One important parameter is the strength of the axial magnetic field produced by a given current. For long solenoids, this value can be determined using the following equation [11]:

$$B_z = \frac{\mu_o NI}{l} \quad (3.2)$$

where  $B_z$  is the strength of the magnetic field along the axis in tesla,  $\mu_0$  is the permeability of free space,  $N$  is the number of windings,  $I$  is the current through the windings of the solenoid in amps, and finally  $l$  is the length of the solenoid in meters. It is also important to determine the power consumed by the solenoid, which therefore needs to be dissipated. This can be found using the following relationships:

$$V = IR \quad (3.3)$$

$$P = VI = I^2R \quad (3.4)$$

where  $V$  is the voltage,  $I$  is the current in amps,  $R$  is the resistance in ohms and  $P$  is the power in watts [26]. The resistance of the wire used was approximately  $30\Omega$ , although it increases as the solenoid heats up. The following table displays the results for some of the currents utilized for experimental runs.

**Table 5.** Magnetic Field and Power for Various Currents

Current (A)	Magnetic Field (G)	Power (W)
5	77	750
6	93	1080
7	108	1470
8	124	1920
9	139	2430
10	155	3000

### 3.3.2 Vacuum Chamber Design and Construction

The next task was the design and construction of the vacuum chamber, which houses all the lenses and voltage connections. The vacuum chamber consisted of a 130 inch aluminum tube which is 4.5 inches in diameter. This tube was able to slide effortlessly into the solenoid. A cap was welded to vacuum seal the tube at the reactor end. This end plug was only 0.25 total inches thick, but a central void was carved into the plug to reduce its thickness to 0.125 inch. This void was 3.5 inches in diameter and 0.125 inches wide. On the

opposite end of the chamber, a flange was applied with a machined groove for an o-ring, which will ensure a vacuum tight seal between connections.

An adapter was also designed so the vacuum system pipe could be connected perpendicular to the beam, as shown in Fig.3.5.

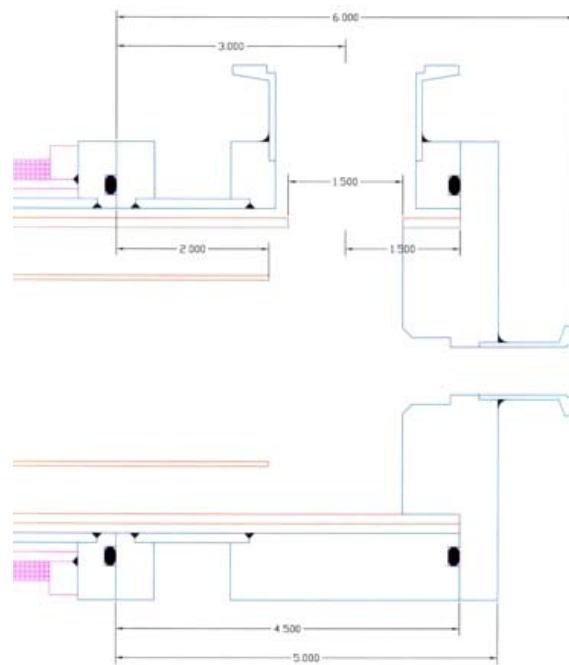


**Fig. 3.5.** Pump adapter<sup>5</sup>

This keeps the vacuum system, which is comprised mostly of stainless steel, out of the neutron headlight emanating from the core. This adapter was simply an aluminum tube with an outer diameter of 6 inches and an inner diameter of 4.25 inches. A 1.834 inch diameter hole is bored out at a 90° angle to the cross section of the adapter. This hole is widened from the top to a diameter of 2 inches, for a depth of a quarter of an inch, to allow for a gasket to connect the adapter to the vacuum system. A KF-50 half nipple is then cut to length and welded to the adapter via this 2 inch shelf. This adapter is then attached to a flange, which is separated from the adapter by 1 inch, which connects to the vacuum chamber.

<sup>5</sup> Courtesy of Dr. William Frieze, University of Michigan

To complete the vacuum chamber, an optics support flange is constructed. This flange seals the vacuum chamber and connects to the lens support tube. This allows the ability to remove the lenses and moderator of the beam without the removal of the entire vacuum chamber. The portion of this flange which seals the chamber is 6 inches in diameter but a shelf which is 0.75 inches wide and 3.75 inches diameter is constructed to allow connection to the lens support tube. This adapter has a hole drilled through the center to allow the connection of the high voltage supplies but these connections will be discussed later.

The vacuum system consisted of a Welch mechanical rough pump and an Alcatel ATP 150 turbo pump. To achieve pressures on the order of  $10^{-6}$  to  $10^{-7}$  torr in the beam with this equipment, the rough pump is used to lower the pressure in the chamber to below 1 torr. Once this threshold is crossed, the turbo pump is cut on to lower the pressure to the micron level. The turbo pump draws air out of the chamber and forces it behind the impeller of the pump. Then the rough pump draws the air away from the rear of the pump. The rough pump is connected to the turbo pump through a valve. The turbo pump is then connected to the vacuum chamber via two 4 foot flexible stainless steel tubes and separated with a gate valve. Quick connectors are used to seal the connections of the flexible hoses. These connectors consisted of a small rubber o-ring with an aluminum inner collar. The o-ring is placed between adjoining pieces and a clamp forces the parts together.

A few problems were encountered in the construction of the vacuum chamber. One involved vacuum leaks in the welded connections. To perform a pressure test, the beam was brought to a certain pressure and checked to see if the pressure is maintained. If the pressure

could not be held, the connections were checked and re-welded as needed, followed by an additional pressure test.

An additional problem involved the selection of o-rings which provide a vacuum tight seal between portions of the beam. Ideally, metallic gaskets would be used for high-vacuum applications. Typically, copper gaskets are used between flanges which contain a stainless steel knife-edge. The bolts on the flanges are tightened uniformly in order to ensure that the knife-edge presses into the copper and forms a tight seal. The flanges for this application were designed to be constructed out of aluminum without a stainless steel knife-edge, in order to keep stainless steel out of the neutron headlight. Metal o-rings were found, but it was later discovered that they required a knife-edge. Eventually, it was decided that ordinary Buna-n o-rings would suffice for short term use with the prototype.

### **3.3.3 Electrostatic Lens Design and Construction**

The final portion of the actual beam to be designed was that of the electrostatic lens system. While the slow positrons have a relatively low spread in energy, they vary a great deal in starting position relative to the centerline of the beam. These lenses serve to focus the positrons into the solenoid for transport out of the biological shield. All the lenses were to be placed inside the lens support tube. The moderator support tube, as described in an earlier section, was designed to contact the walls of the support tube. This served two purposes. One was to ground the moderator, with an additional purpose of allowing the moderator to serve as a support for the lenses.

The original design for the electrostatic lens system of the beam relied heavily on the original Delft design [18], although scaled down by one-third. It was composed of four lenses. The first and third lenses were designed to repel the positrons to the center of the

beam while the second and fourth accelerate the positrons forward through the beam. Figure 3.6 displays this lens design.

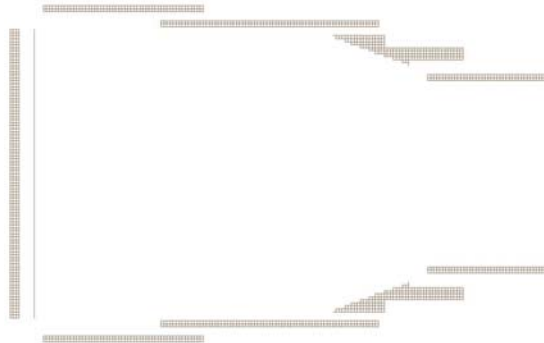


**Fig. 3.6.** Schematic of Delft lens design

This design consisted of four collinear lenses of decreasing diameter. The first lens was separated from the extraction grid by a few millimeters and had an inner diameter wide enough to encompass the active area of the moderator. Each of the remaining lenses overlapped slightly. The third lens away from the extraction grid is tapered by 20°.

Because the beam is composed of concentric tubes, the decision was made to alter the lenses design to compensate for the smaller cross section allowed by the lens support tube, which had a radius of 1.875 inches. Figure 3.7 displays the lens design used for the prototype.

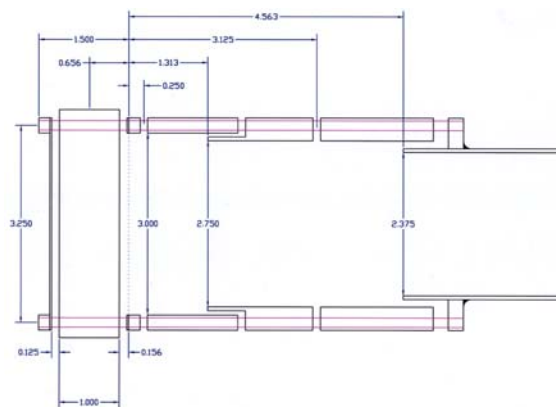


**Fig. 3.7.** Schematic of lens design<sup>6</sup>

<sup>6</sup> Courtesy of Dr. William Frieze, University of Michigan

This design is tubular, each of the first three lenses having the same outer diameter, which was 3.5 inches. Only the first and second lenses, from the extraction grid, and the third and fourth lenses overlap, the overlap being 0.5 inches. The first lens had an inner diameter of 3 inches and the second and third lenses having an inner diameter of 2.75 inches. The first lens had a length of 1.5 inches, the second being 1.75 inches, the third was 1.875 inches and the final lens was 125.69 inches long.

The tubular design aided in the assembly of the lenses. Holes,  $\frac{5}{32}$  inches in diameter, were bored near the outer perimeter through all the lenses and moderator components in a direction parallel to the axis of the beam. These holes allowed the insertion of ceramic tubes which keep the lenses rigid and insulate the lenses for voltage connection by the rods which tighten the assembly. A  $\frac{1}{8}$  inch ceramic spacer was placed between each component of the electrostatic lens assembly. The first component placed on the ceramic rods was the repelling plate, followed by the moderator, extraction grid and finally the four lenses. Because the fourth lens had a diameter of only 2.5 inches, a small collar had to be added to allow for this lens to be attached in a fashion similar to the previous components. To adhere the components together, a piece of the aluminum wire was straightened and threaded at the ends. These small aluminum rods were then inserted into the ceramic tubes. The lens and moderator assembly was then tightened with small nuts at each end of the rods. Inside the fourth lens, an aluminum plate, which almost covers the entire cross section, is positioned approximately 8 inches from the far end of lens four, approximately 123 inches from the moderator. This plate served as a target for positrons to annihilate.

A ceramic support was designed for the opposite end, away from the moderator, of lens four. This support would serve to center this end of the beam in the lens support tube.

The support was fabricated so it would fit exactly into the end of lens four and also extend past the lens to contact the walls of the lens support tube. This support also serves to direct the high voltage connection wires from the vacuum feedthrough on the optics support flange, through the support and to the lens assembly.

### **3.3.4 Beam Assembly**

Once individual components were completed, the beam was prepared for construction. The first task was to clean any component that would exist inside the vacuum chamber. Anything inside the vacuum chamber, including the inner walls of the vacuum chamber, needed to be cleaned to remove dirt and water from inside the beam. This task is necessary because contamination, especially water, will constantly stream off the walls and reduce the effectiveness of the vacuum in the chamber. Solvents, which evaporate quickly, are needed to clean parts because the introduction of water will pollute the vacuum. Liquid water will sublime off the walls as the pressure decreases. After the parts are clean, they are rinsed in acetone to remove any traces of water and grease. Smaller parts could easily be cleaned by hand, but larger parts, such as lens four and the vacuum chamber, needed special attention. A ramrod was constructed and these larger parts were cleaned with water. Next, the ramrod was used to clean with acetone.

Aluminum wire inside ceramic tubes was used to connect the electrostatic lenses to the ceramic support at the opposite end of the beam. Once wiring was completed and tested, the lens system was inserted into the lens support tube and was attached using screws through the tube and into the moderator assembly. The lens support tube was then attached to the optics support flange. This completes construction of the actual lens assembly. The lens assembly could then be slid into the vacuum chamber and the chamber sealed. The

vacuum chamber was backfilled with dry nitrogen to prevent any degradation to the moderator during transport from the University of Michigan to North Carolina State University. The vacuum chamber was slid into the solenoid and construction of the beam was complete, a picture of the completed beam is shown below. A clear plastic cup at the left end covers the delicate wires of the high voltage vacuum feedthrough.



**Fig. 3.8.** Final assembly of beam

### **3.4 Shielding Construction**

The beam port selected for use of the positron facility was beam port 6, the 12x12 inch beam. To begin construction, the core was dismantled to remove the contents away from the beam ports. The beam port was drained, opened, and the contents, beam plugs, were removed to prepare it for the addition of the beam insert. Figure 3.9 is an image of the evacuated beam port before construction.



**Fig. 3.9.** Empty beam port 6

An aluminum insert was first constructed to reduce the 12x12 inch square beam port to a circular beam port with an inner diameter of approximately 6 inches. The insert consisted of a 6 inch Schedule 40 aluminum pipe. One end of the pipe was cut at an angle of 37°, and sealed by welding an aluminum plate to the opening, so the insert could sit flush against the surface of the beam port at the core. To support the tube, the insert rested on an aluminum stand which was slid into the beam port. Figure 3.10 displays the aluminum insert sitting on the stand.



**Fig. 3.10.** Beam port insert on aluminum stand

Lead was stacked around the insert, as can be seen in Fig.3.11a, to fill the entire port for the last couple of feet, in order to provide some additional shielding and support for the outlet of the beam. The next task was to seal the beam making it water tight. An aluminum plate was constructed, which slid over the beam insert, and attached to the wall of the biological shield using the same holes which held the previous cover. A rubber gasket was used between the cover and the biological shield making it water tight. An o-ring and collar

was then used to seal the opening between the insert and cover. Once the installation of the insert was complete, it was cut down to its final desired length. The beam port was then flooded, effectively reducing the 12x12 inch beam port to a 6 inch circular beam port.



a)



b)

**Fig. 3.11.** Images of the beam port insert; a) placed within the beam port, b) completed beam port insert

The base of the shielding was constructed before the insertion of the prototype positron beam to prevent the possibility of damage that may arise by stacking shielding while the prototype was in place. Figure 3.12 shows the initial construction of the beam shielding. It displays the initial layers and a shroud of polycarbonate, which covers the actual beam. The base simply consisted of concrete blocks. It was four rows tall, approximately 16 inches high, and extends six columns, or approximately 36 inches, to the left of the outlet of the beam. The shielding on the right simply connects to the neutron imaging facility already in place. A layer of lead was placed upon this concrete base. It consists of three layers of lead and has dimensions of approximately 24"x48"x6". These two layers effectively completed the base of the shield.

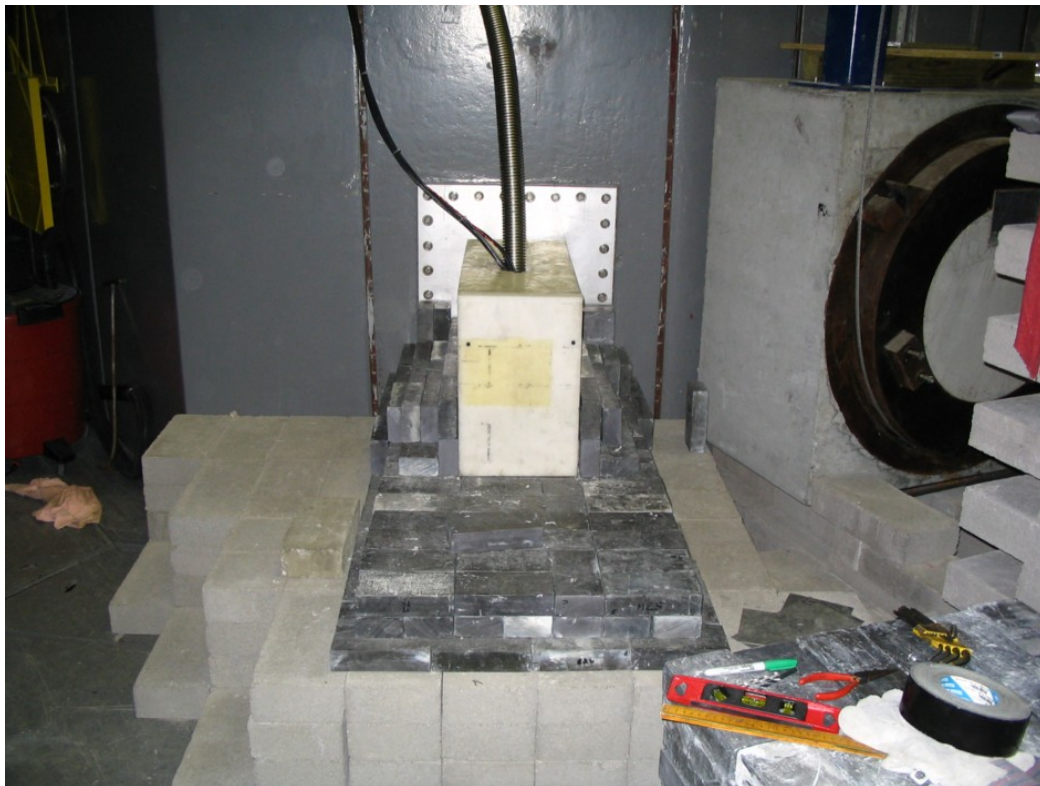


**Fig. 3.12.** Construction of base of the shielding

Now that these base layers were completed, it was time to prepare the positron beam for insertion into the beam port. Before insertion, a cadmium cap was placed around the moderator end of the beam. The cap was wrapped around the solenoid support tube. As stated previously, the cadmium cap acts to absorb neutrons and emit high energy gamma rays. To cover the cross section of the beam, a circle with tabs was cut from a 0.5 mm cadmium sheet. These tabs were then folded over the support tube. To further cover the moderator, and to hold the cross sectional cap, a thin strip of cadmium, approximately 2 inches wide, was wrapped around the tube and fastened with wire. Marks had to be placed on the outside of the solenoid as a reference for where the face of the target on the inside of the beam was located. This information was needed for future reference for alignment of the collimators for the detectors. The target was approximately 5.875 inches from the end of the solenoid flange. With the addition of these reference marks, the positron beam was now prepared for insertion into the beam port.

Borated Polyethylene was used to encompass all external portions of the beam. This material has the ability to thermalize fast neutrons and absorb neutrons. Figure 3.13 is a close up picture of the beam sitting inside the polyethylene layer. One layer, 2 inches thick and 10 inches wide, was placed below the beam and was allowed to extend approximately 1 foot past the end of the beam. The walls were constructed of two sheets of the polycarbonate, providing approximately 4 inches of shielding. To construct the sides of this cover, marks were placed on the polycarbonate to indicate where the collimators should be located. The dimensions of the opening width for the collimators were approximately  $\frac{5}{16}$  inch through the first layer, i.e. the layer closest to the beam, and  $\frac{5}{8}$  inch for the second layer. The height of the collimator opening was approximately 4 inches. To complete this

polycarbonate layer, 2 layers were placed in front of the beam and the top was constructed. The top of this layer needed an opening to allow for the high voltage connections and flexible vacuum tube to pass through and connect to the beam. An approximately 2 inch in diameter hole was drilled through both layers of the top.

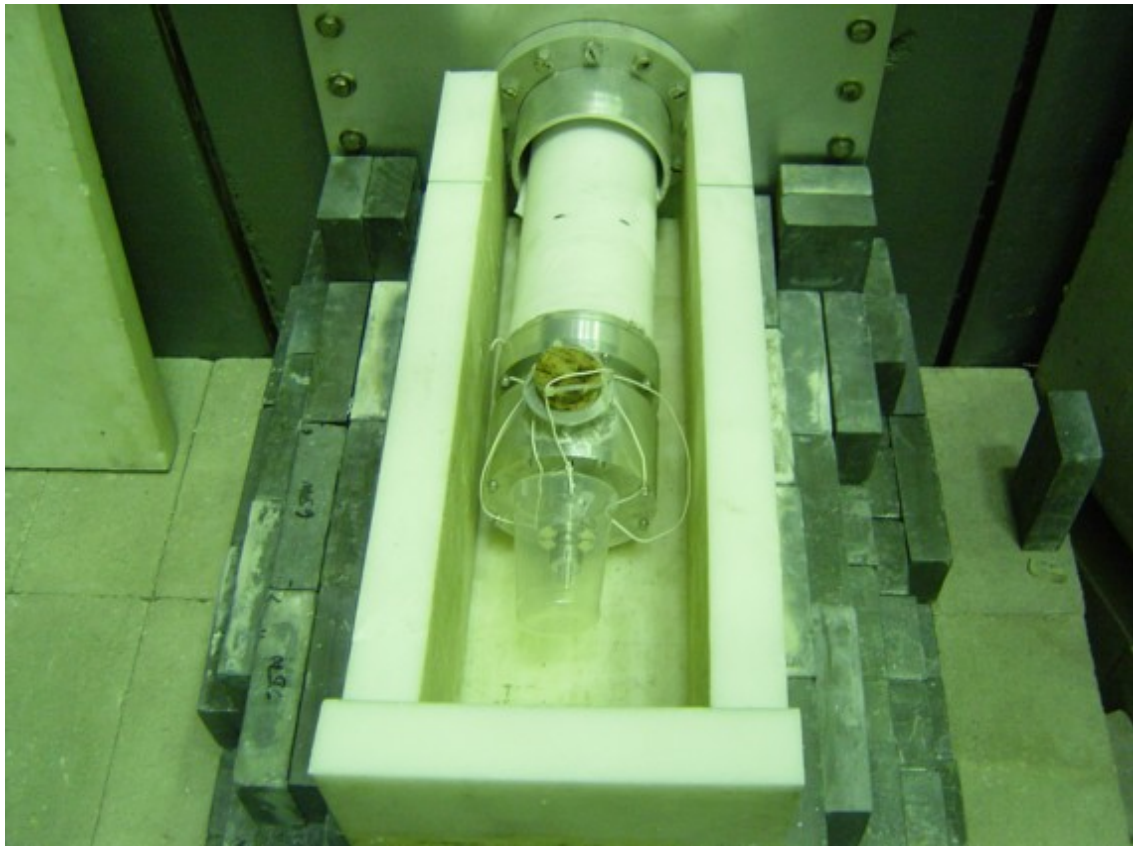


**Fig. 3.13.** Close-up of borated polyethylene layer

Lead and concrete was stacked around this polyethylene layer to provide final shielding. The lead plug initially removed from beam port 6 was placed directly behind the beam, as seen in Fig.3.14. In this figure, the lead plug is wrapped in yellow plastic to protect individuals from contamination from contact with it. Lead was stacked around these inner layers and the cables and vacuum hose. The sides of this layer were composed of approximately 8 inches of lead. Lead extended in front of the polycarbonate layer by approximately 2 feet.

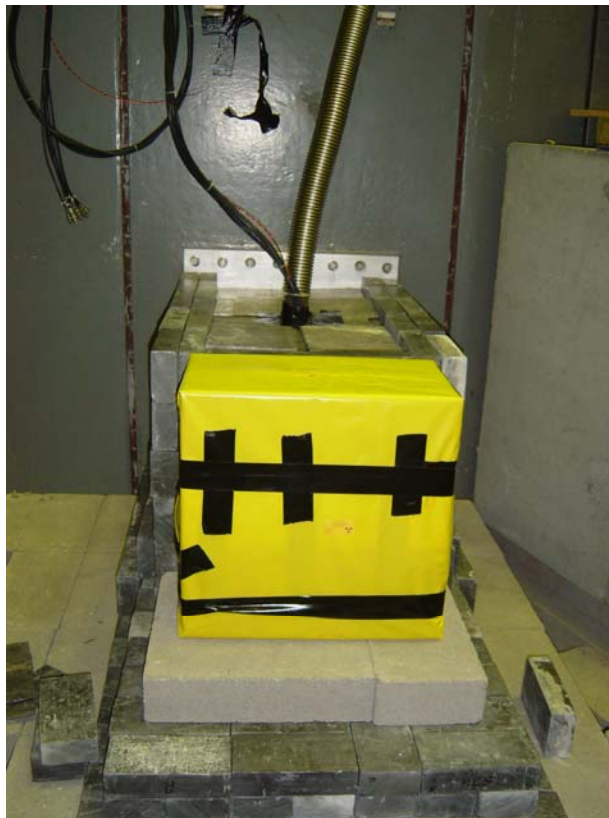


**Fig. 3.14.** Images of lead layer; a) front view, b) side view

Concrete was then stacked around this lead layer. As the walls rose, an area needed to be set aside for the placement of the detectors. Once the walls reached the height of the collimators, the detectors were set in place and lead was stacked around them to try to reduce the background, as pictured in Fig.3.15.

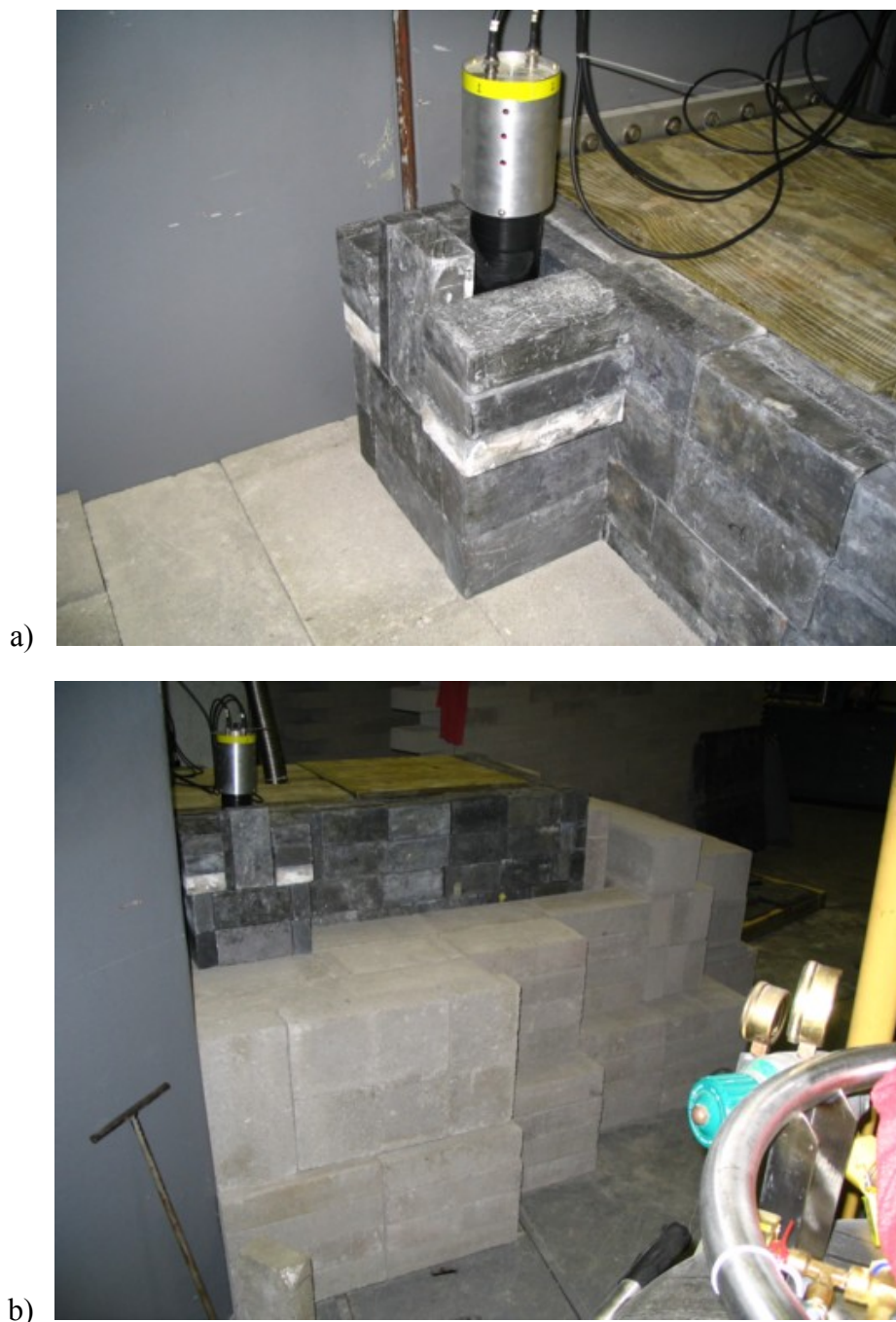


**Fig. 3.15.** Images of detector placement; a) close-up, b) side view

After the detectors were placed in their final positions, concrete blocks were carefully stacked to complete the shield. Figure 3.16 displays the shielding as it appeared as testing began. A concrete façade was eventually constructed, which allowed the construction for a stable floor on top of the shielding to hold the electronic equipment and the vacuum system. Pictures of the final shielding can be seen in Fig.3.17.



**Fig. 3.16.** Initial shield setup



**Fig. 3.17.** Completed shield

## Chapter 4

### Testing and Results for Prototype

#### 4.1 Introduction

Once shielding was completed, tests could finally begin to determine the number of positrons produced by the moderator/convertor. Detectors, which were now contained within the shielding, were connected to electronics and brought to their operating voltage. A small, but measurable, count rate of positrons could be detected as the core was being loaded.

#### 4.2 Electronic Setup

The annihilation of the positrons on the aluminum target will result in the production of a pair of back-to-back 511keV gamma rays 99.7% of the time. This fact was utilized to determine the number of slow positrons produced [13]. A schematic of the detection setup is shown in Fig.4.1.

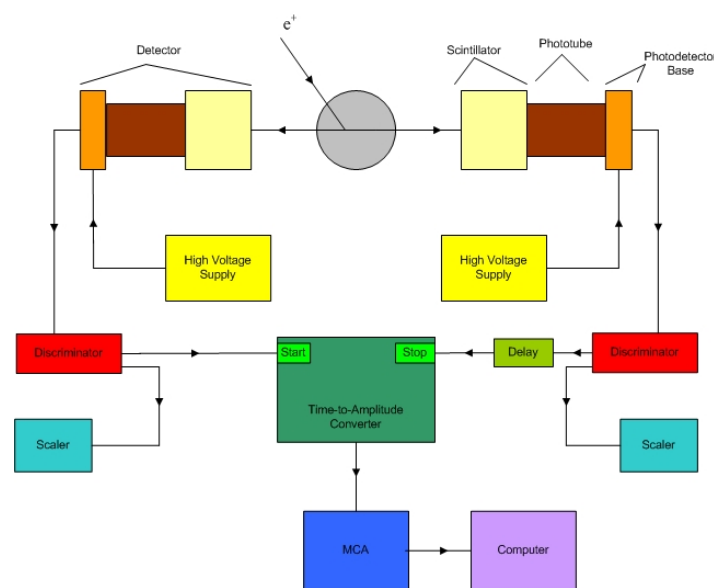
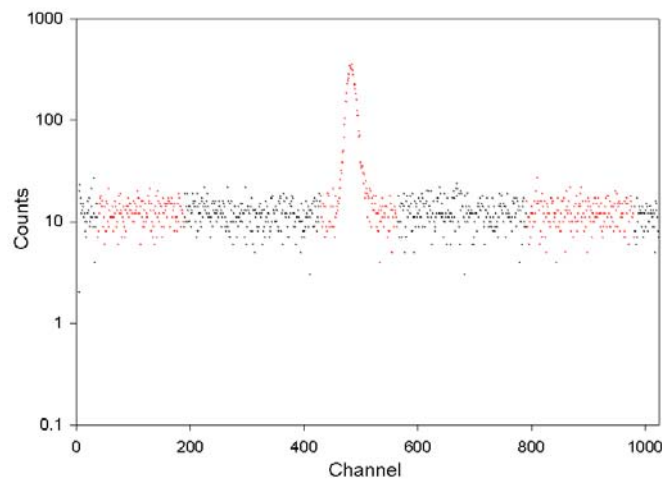


Fig. 4.1. Schematic of slow positron detection electronics

Two detectors, one 4x4 cylindrical and one 5 inch cubical plastic scintillators, are placed on opposite sides of the annihilation target, separated by 1 meter. A fraction of the annihilation events will be detected by both detectors within a 50ns time window, which will appear in a region that corresponds to two events at the same time and gives rise to a prompt coincidence peak. A delay is placed in the stop branch of the detection system to shift the spectrum to the right by an amount equal to the delay. If no delay was present, the peak would be centered at channel zero, meaning only half the peak would be measured. If there is slight variation in the time which an event is detected in each detector, the peak will widen. If the signal in one detector varies drastically from the other, the prompt peak will be asymmetric. If there is amplitude walk in the stop branch of the timing signal but little to none in the start, the prompt peak will contain an asymmetric tail with longer time differences [27]. For the setup used, the signal from each detector proceeds to its own discriminator, which continues to a Time-to-Amplitude Converter (TAC). The time difference of the signals is then converted to a pulse, which is sent to a MCA to produce a coincidence time spectrum, as seen in Fig.4.2. In the figure, the red areas far to the left and right of the central peak delineate the portions of the continuum used to correct for background under the central peak.



**Fig. 4.2.** Coincidence spectrum taken at reactor power level of 10kW

The peak produced is due to the “true” coincidences between the signals of the detectors. Sections of the flat region of background continuum to the left and right of the beam were utilized to correct the peak area for background events and determine the net peak area. To do this, a sum of the background areas is multiplied by a factor which equals the number of channels in the peak region divided by the sum of the channels in the background regions.

The net peak area determined above is however only partially due to slow positron annihilation events; there is an additional background of annihilations due to fast, unmoderated positrons. To determine the true number of slow positron annihilation events detected, a positron beam-on run, meaning slow positrons were being focused and transported to the annihilation target, was performed which was then followed by a beam-off run. To turn off the beam, the voltages on the repelling plate and withdrawing grid are reversed, which pulls slow positrons away from the solenoid, therefore, the beam off peak should be solely composed of the annihilation of fast positrons. The true number of slow positrons detected would then be the corrected beam on peak minus the corrected beam off.

### ***4.3 Detection Efficiency***

Detector efficiency can be classified into two categories; absolute and intrinsic efficiencies. Absolute efficiency depends on both detector properties and the geometry of the detection setup. Intrinsic efficiency depends mainly on the properties of the detector and source, geometry having little influence [27].

To calibrate the detection efficiency, a special calibrated source was used. It was placed in a holder, which positioned the source in the exact position of the annihilation target. The source used was Germanium-68, Ge-68, created on December 15, 2004 and had an initial strength of 10.51  $\mu\text{Ci}$ . By knowing the date of creation and the initial strength, the

strength of the source at the time of the measurement can be determined. The activity of a radioactive source after the passage of time is given by the equation:

$$A(t) = A_0 e^{-\lambda t} \quad (4.1)$$

where  $A_0$  is the initial activity and  $\lambda$  is the decay constant, which equals  $\ln(2)/t_{1/2}$  [28]. The half-life of Ge-68 is found to be 270.8 days and decays via electron capture [29], which occurs in a neutron deficient nucleus where an atomic electron interacts with a proton to form a neutron [28]. The date of the efficiency calibration test was March 1, meaning 75 days had elapsed since creation of the source. The activity was then found to be 8.67  $\mu\text{Ci}$ , or 321 kBq. The positrons are created from the decay of the daughter nuclide of Ge-68, Gallium-68, which emits positrons 89.04% of the time and has a half-life of 68 minutes [23]. Because the half-life of Ge-68 is so much greater than that of Ga-68, gallium assumes the activity of the germanium after a short period of time, therefore the emission of positron annihilation events is equal to 89% of the activity of the source, which corresponds to 290,000 positrons per second.

The peak generated by the Ge-68 when placed in the position of the aluminum annihilation target produced a count rate of 50 Hz. The maximum positron rates measured at 10kW was 40 Hz, corresponding to a scaled positron rate of 232 kHz. A factor of 0.8 must be introduced to the germanium source test to account for the smaller attenuation brought about because two aluminum tubes, lens 4 and the lens support tube, were removed to allow the insertion of the source holder. This would reduce the detected count rate for the source to 40 Hz; therefore the scaled positron rate would increase to 290 kHz. Another factor of 0.89 must also be introduced to the source test to allow for differences in attenuation of the source

holder and the annihilation target. The final efficiency of the detection setup is therefore  $1.2 \times 10^{-4}$ .

#### 4.4 Initial Tests

Data collection began as soon as the loading of the core was complete. At this point, the only gamma rays incident on the moderator were created from the decay of long-lived fission fragments. While the count rate was small, the data demonstrated two important results, that the moderator can successfully convert gamma rays to slow positrons and the electrostatic and magnetic lenses were controlling and transporting the positrons.

Once the core was fully loaded and initial tests were completed, a series of runs were performed at varying power level, the results of which can be seen below.

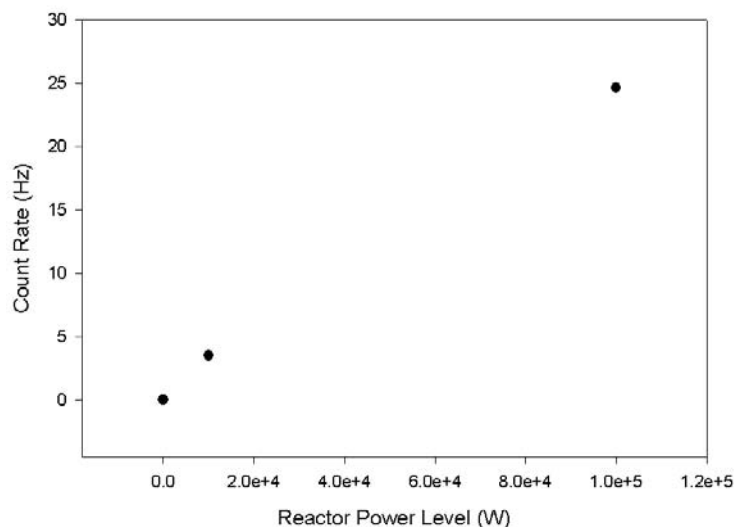


**Fig. 4.3.** Count rate vs. power level

Data points were taken at reactor power levels of 0W, 50W, 10kW and 100kW. Power levels above 100kW were not allowed because the neutron dose rate at the top of the shield was beginning to reach unacceptably high levels. This was probably due to holes placed in the shielding which allow the passage of the vacuum tube and electrical connections to the

positron beam and solenoid. Also, the count rate seen by the detectors at higher power levels would have been too great for the TAC based electronics used for detection, the dead time at 100kW was over 30%.

It can be seen that the data seems to follow a near linear trend, relating power level to count rate. This allowed the assumption that data taken at a particular power level could be scaled to higher power levels. The decision was made to take data in future runs at a reactor power level of 10kW. At this 1% power level, the detection set up had a small amount of dead time and the results could be scaled to full power, which would tell what the count rate for a completed beam would be when operating at full power.

These initial tests unfortunately exposed a possible problem with the beam. The detected count rate at 10kW was approximately 3.5 slow positrons per second, but this only scaled to a count rate of approximately  $10^6$  slow  $e^+$ /second at full power. The desired count rate from this beam was closer to  $10^8$  slow  $e^+$ /second. Initially this was attributed to a problem with moderation and initial plans were made to test the moderation efficiency of the Tungsten tubes of the moderator.

#### ***4.5 Magnetic Transport Efficiency***

Before testing of the moderation efficiency of the tubes began, the idea was proposed to test the magnetic transport efficiency of the beam. By altering the current flowing through the solenoid, differing axial magnetic fields could be produced. The tests were to understand what effect the strength of the magnetic field had on the transport of the slow positrons, the expectation being there would be no effect. Current was varied from 0 A to only slightly greater than 5 A. Although the power supply had the potential output of 10 A of DC current, approximately 5 A was the greatest amount which could be output due to the resistance of the

wire and the maximum voltage available of 150 V. To take the measurements, a five minute beam on run was performed immediately followed by a 5 minute beam off run. The current output of the solenoid was altered and then the measurement process was repeated. The results for the initial tests of this hypothesis are represented by the black plot in the Figure 4-4, which plots the count rate of positrons scaled to full power against the magnetic field of the solenoid. To scale the detected count rate to the scaled count rate at full power, the following equation was used.

$$\text{Scaled Count Rate} = \frac{\text{det ected count rate}}{\text{counting duration}} * \varepsilon^{-1} * 100 \quad (4.6)$$

where  $\varepsilon$  is the detection efficiency,  $1.2 \times 10^{-4}$ , and the factor of 100 scales the power from 10kW to 1MW.

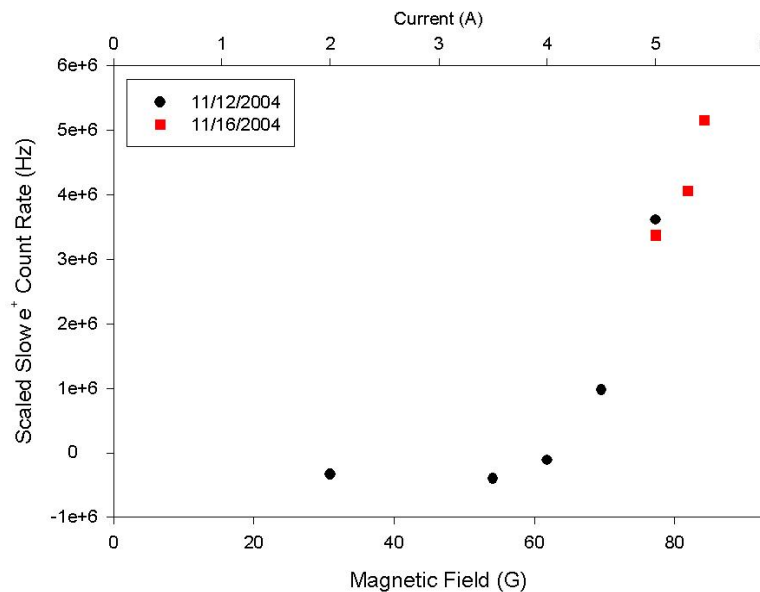


**Fig. 4.4.** Count rate vs. magnetic field

As can be seen, the magnetic field seems to greatly influence the transport efficiency of the beam. After seeing the influence of the field strength on the efficiency, the solenoid was run at its maximum possible current the power supply could provide to see if the trend held. The results can be seen as the red plot in Fig.4.4.

The direction of the field was then reversed to see if that parameter had any influence on the efficiency. Runs were performed at a 5 amp current, producing an approximately 75 G field, in both the original configuration and in a configuration which had the leads reversed. The results of this effect on the scaled positron count rate are summarized in the Table 4-1.

**Table 6.** Count Rate with Differing Magnetic Field Orientation

Original Direction	Reversed Direction
$3.4 \pm 0.3$ MHz	$8.1 \pm 0.3$ MHz

The results in this reversed direction, which will now be called the favorable direction, seemed to be more than twice that of the original orientation. Due to these results, tests were again performed to see the influence of varying the magnetic field in the favorable direction and obtaining the scaled count rate, the results of which can be seen below.

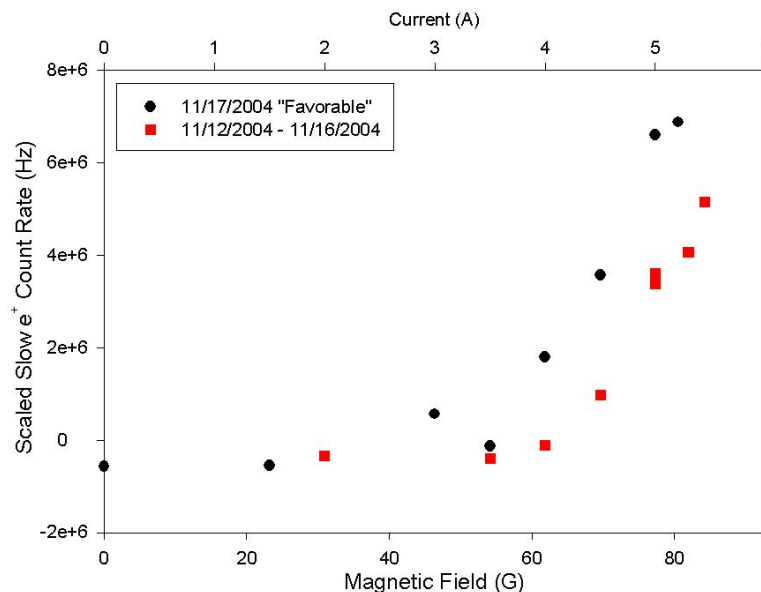


**Fig. 4.5.** Count rate vs. magnetic field in favorable and original magnetic field orientation

The influence of the of the magnetic field seems to still be following the trend that increasing field increases the scaled count rate, although the change in the direction of the field seems to have doubled the amount of positrons successfully detected.

Once the previous tests were concluded, the setup used had reached its full potential. An additional power supply was needed to see if the count rate trend continued or came to a peak. An identical power supply was purchased and connected in series with the first, which then allowed DC current output of up to 10 A. The solenoid was not designed to run with current levels much higher than 5 A, so the beam had to be allowed to cool periodically to prevent damage to the solenoid. The beam could run for an hour at 6 A before needing to be cool. It could run for 30 minutes at 7 A, but only 10 minutes at 8 A. At power levels above 8 A, the beam was allowed to cool after every five minute run.

Now that higher current levels were available, runs were once again performed to see if higher current levels continued to result in higher count rates. The results can be seen in Fig.4.6.

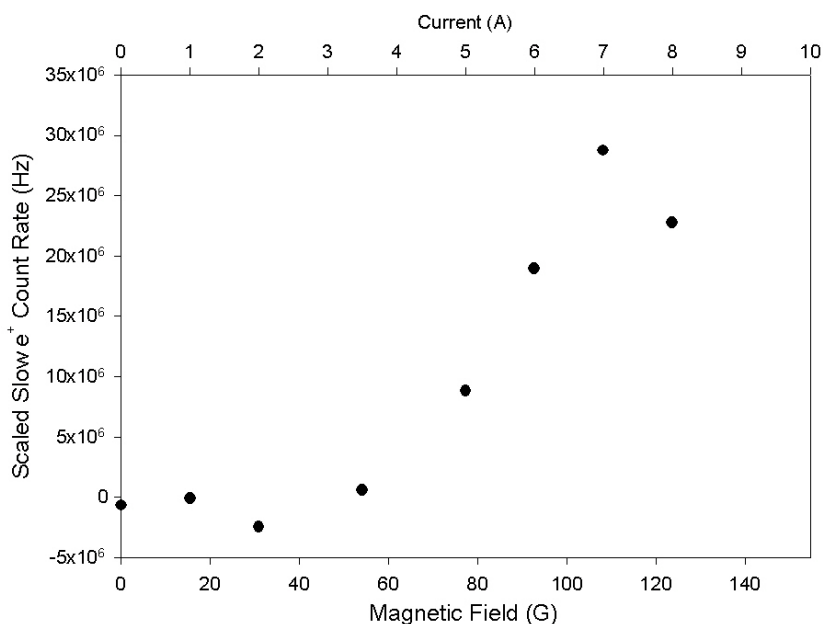


**Fig. 4.6.** Count rate vs. magnetic field with higher current levels

The peak scale count rate found was determined to be  $28.7 \pm 0.4$  MHz, which occurred at approximately 110 G, or at a current of 7 A. The results seemed to peak, so the tests needed to be repeated to determine if the count rate comes to a peak or if the rate stabilizes at a

plateau. Unfortunately, the data taken over the next two trials provided confusing results, which can be seen in Fig.4.7.

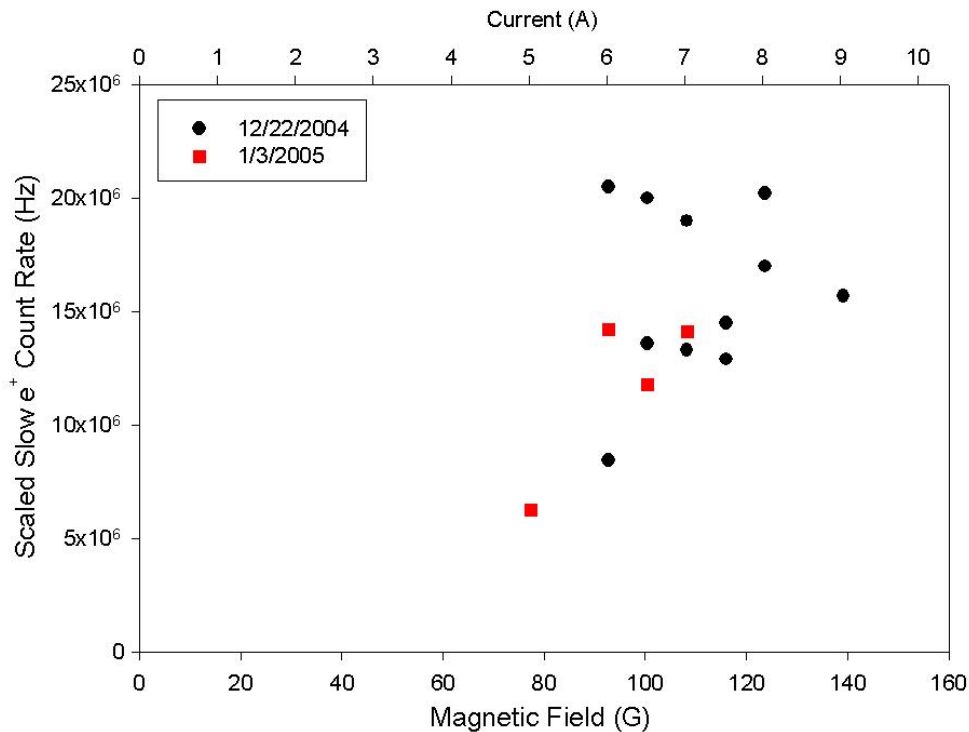


**Fig. 4.7.** Data taken which shows no trend or control

There does no longer appear to be any trend in the data and the measurements cannot be reproduced. It was then noted that the count rate does not appear to be constant during the counting period, i.e. the count rate detected would slowly decrease over the counting period. The decision was made to allow the beam to stabilize before counting began. For the next set of measurements, the beam was allowed to stabilize for two minutes every time a change was made in the lens voltages or the magnetic field. With the stabilization, a trend similar to the ones seen previously, in Figure 4-6, can again be seen, although it appears to be shift so that the maximum count rate occurred at 9 A. These results can be seen in Fig.4.8.

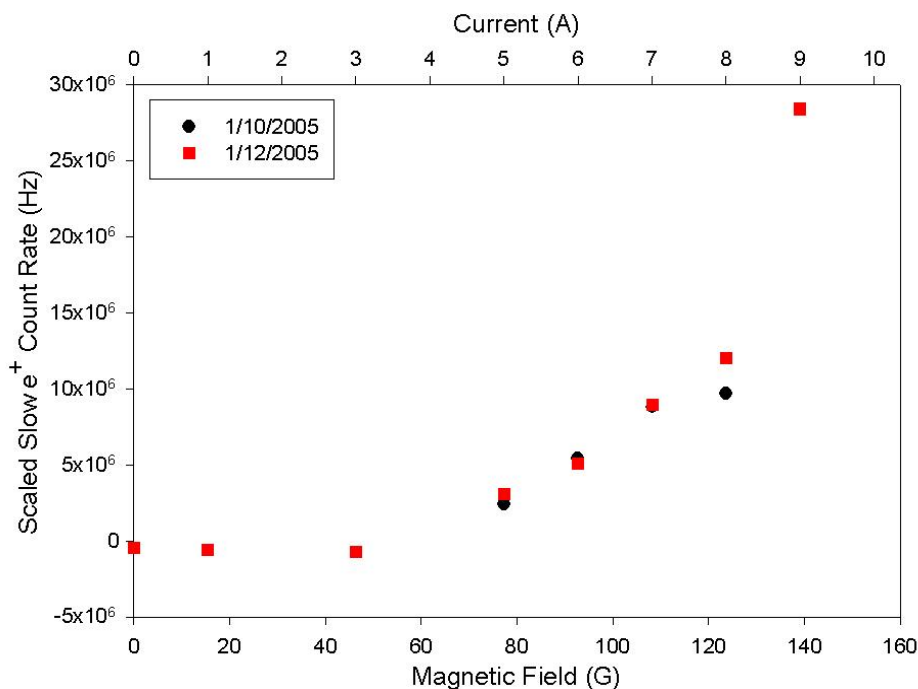


**Fig. 4.8.** Count rate vs. magnetic field with 2 minutes of stabilization

The peak at a current of 9 A was  $28.4 \pm 0.4$  Hz, but the scaled count rate at 7 A was only  $9.0 \pm 0.3$  MHz, approximately 30%, of the original scaled count rate.

To explain the loss in signal, the idea was proposed that heating of the solenoid was causing the aluminum beam pipe to expand, which pushed the annihilation target out of the view of the collimators. The thermal expansion coefficient of aluminum is  $23.8 \text{ ppm}/^\circ\text{C}$  [30], which relates to  $0.007 \text{ cm}/^\circ\text{C}$ . If the temperature were to change by  $100^\circ\text{C}$ , the target could move 7mm. This is rather significant considering the width of the collimators.

It was desired to perform runs which would minimize the effect of heating of the solenoid by running in a pulsed mode. Initially, a 100 second beam on run was performed followed by 10 minutes of cooling time with the solenoid off and then the beam off run was performed. After obtaining the results of these trials, runs were performed with 100 second runs, for both the beam on and beam off, with cooling times of 30 minutes in between each half run. The results of these trails can be seen below.

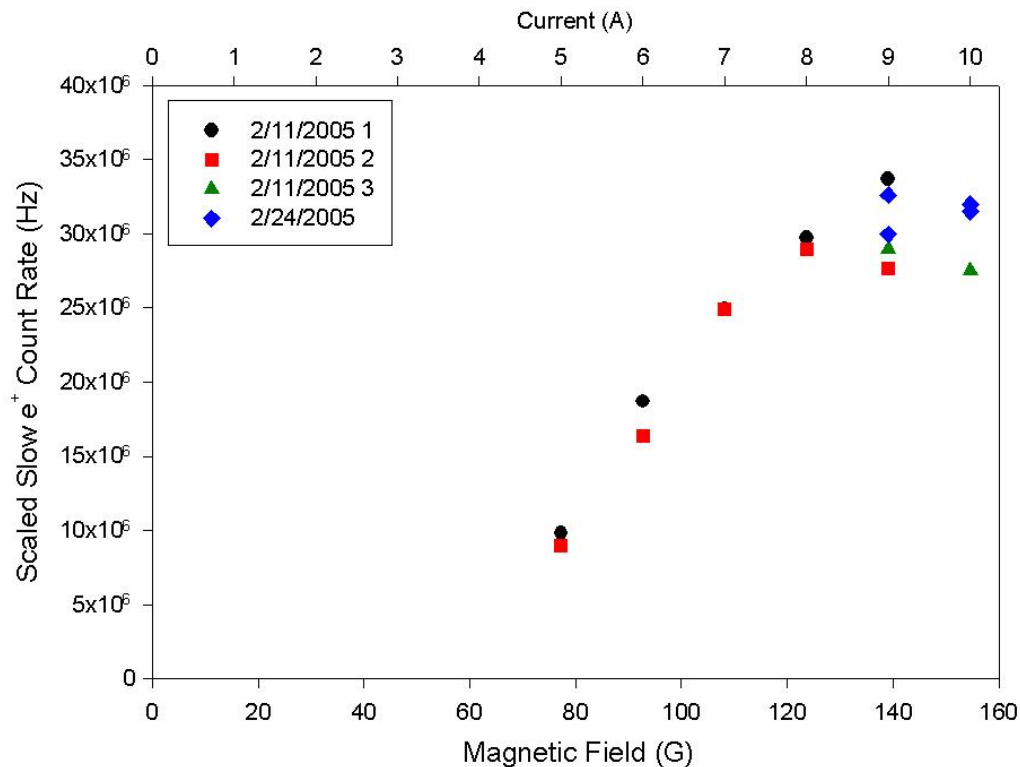


**Fig. 4.9.** Count rate vs. magnetic field with cooling periods and no stabilization

The data acquired on February 11, 2005 corresponds to trials with 10 minutes of cooling between half runs; the 1, 2, and 3 corresponds to which series the data was taken in. The data which was taken on February 24, marked with green, corresponds to tests with 30 minutes of cooling between half runs. The 7 amp value was up to  $24.9 \pm 0.3$  MHz, or it was back up to 87% of the value initially determined. The highest scaled count rate recorded by the prototype positron beam was  $33.7 \pm 0.4$  MHz, which occurred at a solenoid current of 9 A.

#### 4.6 Final Prototype Tests

Once counting tests which allowed extended periods of cooling time were completed, the removal of the shielding was necessary to complete final testing. These tests included the use of a calibrated radioactive source to calibrate the detection setup, followed by tests that show the effect of moving the target without having to turn on the solenoid. It was also

desired to map the magnetic field of the beam port to find any residual magnetic fields that may be deflecting the positron beam during transport.

#### 4.6.1 Source Location Tests

Additional tests were performed with the Ge-68 radioactive source to determine the effect of moving the target on the detection efficiency. The source holder was placed on an aluminum bar which passed through the end of the beam. This allowed the movement of the source forwards and backwards by 1/8 inch increments, the zero location being what is believed to be the location where the annihilation target was. The exact location of the source within its 1/4 inch thick plastic holder was not known, therefore the tests were performed twice, one with the label on the source facing away from the holder and one with the label facing the holder. The results of this test can be seen below; the FWHM of both curves is approximately 1 cm.

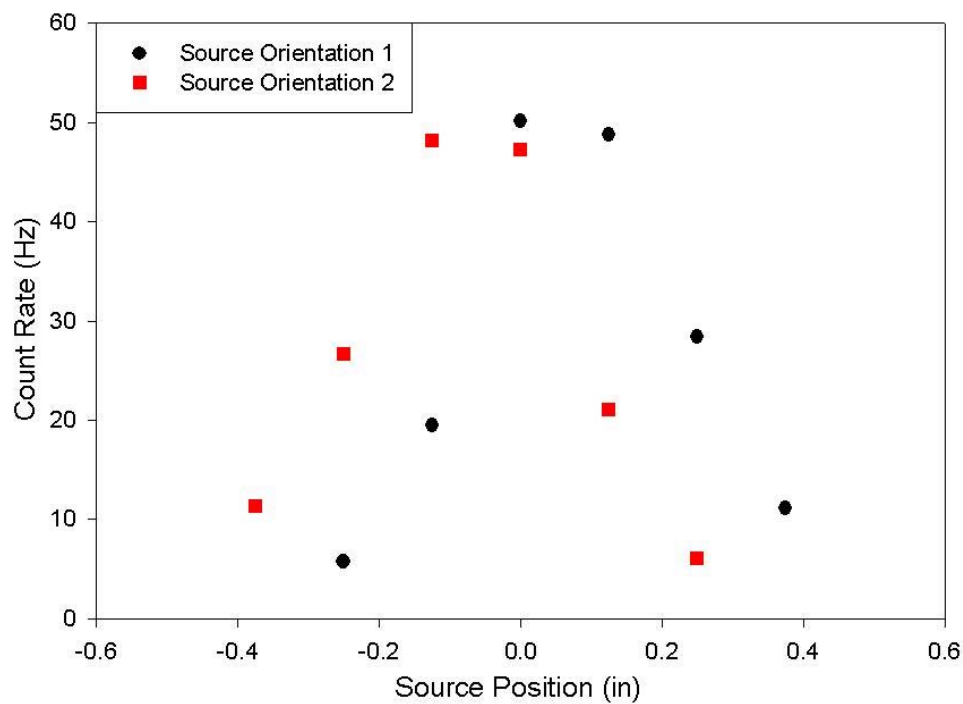


**Fig. 4.10.** Count rate vs. position of Ge-68 source

As can be seen, the source was not exactly centered in the collimators. According to the results, the target seemed to be off center by approximately 1/16 of an inch or less.

The source was then placed back in the zero position and tests were performed to see what effect heating caused by the solenoid had on the number of counts detected. To test this effect, the current through the solenoid was set and counts were taken for 30 seconds, followed by 30 seconds of waiting. This allowed one data point to be taken every minute. The results of these tests can be seen in Fig.4.11.

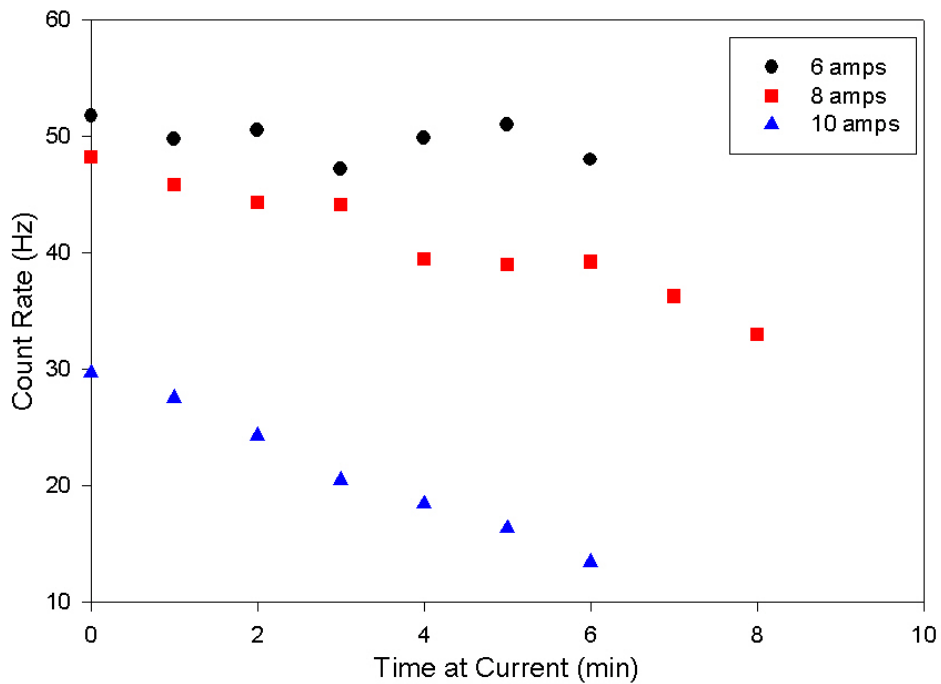


**Fig. 4.11.** Effect of solenoid heating on count rate

At a current of 6 A through the solenoid, the count rate seems somewhat constant, although the count rate does seem to slowly decrease. The effects are more drastic at 8 and 10 A. The count rate drops approximately 30% over 8 minutes at 8 A and drops nearly 50% over 6 minutes of operation at 10 A. The beam was warm to the touch once tests were over and did not quickly cool. After more than an hour and a half of cooling, the count rate was still 16.6

$\pm 0.2$  Hz, or only 32% of the initial count rate taken with a cold solenoid. This result is consistent with the earlier estimate of 7 mm of displacement of the target.

#### 4.6.2 Mapping of Residual Magnetic Field

The final tests performed on the prototype positron facility involved mapping the magnetic field of the beam port used. It was desired to determine if there were any residual magnetic fields, both axial and transverse, within the beam port. These fields could deflect the positron beam and cause them to impact the walls of the electrostatic lenses and not reach the annihilation target. To do this, a Hall probe magnetometer was attached to an apparatus which could slide in the beam port. The Hall probe was slid to the rear of the beam port insert, the core end, and was pulled out in 2 inch increments. This was performed for the axial field and the horizontal and vertical transverse field. The results of these tests can be seen in Fig.4.12.

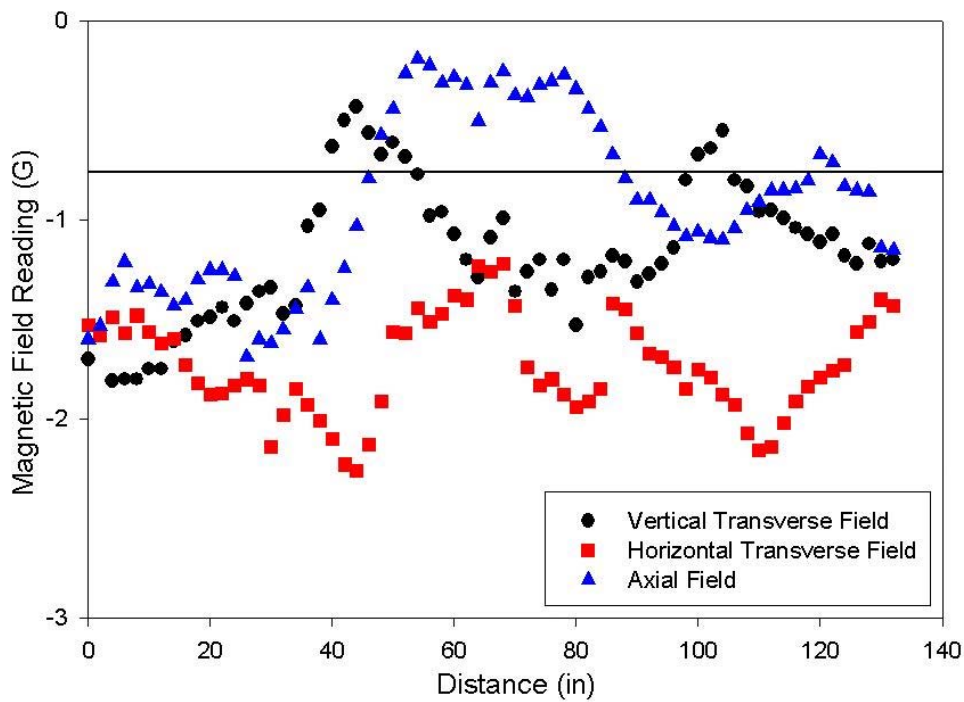


**Fig. 4.12.** Horizontal and vertical transverse and axial magnetic fields within the beam port

The horizontal black bar at approximately -0.76G represents the calibrated zero field reading for the horizontal and vertical transverse field measurements. The zero for the axial field occurs at approximately -0.56G. While the changes in the fields are not drastic, this data plot demonstrates that there are changes at approximately the same position in the beam port. For example, there appears to be a change, either positive or negative, in the magnetic field at approximately 30 inches away from the end of the beam port insert. Changes in all three fields can again be seen at approximately 80 inches away from the core end of the beam port. Using an AutoCad drawing of the reactor, the variations in the field appear to begin somewhere in the pool and continue throughout the entire beam port. There are also 7/8 inch diameter iron reinforcing rods within the structure of the concrete biological shield, which could be magnetized and/or alter the field when the solenoid is operating. Note that a one G transverse field over the 120" beam length with axial field about 100 G shifts the beam center off axis by 1". This would account for the positron rate increase with increasing solenoid current and indicates the importance of magnetic shielding in the actual positron beam to be built.

## Chapter 5

### Conclusions and Future Work

#### 5.1 Conclusion

The purpose of this research was to design and test a prototype design of an intense positron beam for use in the PULSTAR Reactor at North Carolina State University. This endeavor proved to be a success, producing what would be a count rate of 33 MHz at a power level of 1 MW of reactor power. The electrostatic lens system was able to withstand the intense radiation produced by the reactor, which could be seen by the fact that there was no arcing detected in the voltages, even at full reactor power.

Optimization of the core configuration could help to further improve the photon flux across beam port 6. If the reflector were switched to the right side of the core, the total photon flux could increase by a factor of 2. Figure 5.1 displays the photon flux for this optimized core flux against the flux produced by the core arrangement used for the prototype beam, without the addition of cadmium.

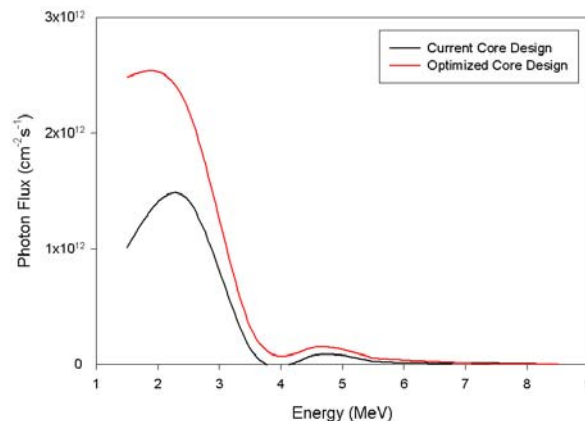


**Fig. 5.1:** Comparison of photon fluxes for current and optimized core arrangements

If the optimizations in the core configuration were implemented for this prototype, the scaled slow positron count rate could be as high as 66 MHz.

While heating proved to be an issue for this prototype, it will not be a problem for future work. In retrospect, expansion effects should have been expected at higher solenoid currents. The solenoid was designed to operate at a current of only 5 A and was pushed with a current of 10 A. The effective heat insulation of having a solenoid in a beam port also caused the beam to retain heat for long durations of time. The final positron facility will not rely on the use of collimators for detection. If a lifetime facility is constructed, the start and stop signals will be utilized, rather than the detection of collinear photons.

The prototype beam also demonstrated that magnetic shielding should be used to reduce the residual magnetic field. While the changes in the magnetic field were not great, any perturbations in the field could alter the trajectory of the positrons, possibly causing them to impact the lenses. Magnetic shielding will also prevent magnetization of iron rebar that is present in the structure of the biological shield.

## **5.2 Future Work**

### **5.2.1 Bending of Beam**

The next major task is the bending of the beam to remove it from the neutron headlight coming out of the port. This will prove to be difficult machining. The long electrostatic lens, the drift lens or lens 4, must be bent, along with the solenoid. Not only will the components need to be bent, but the drift lens must be centered in the axial position of the beam to prevent positrons from impacting the lens. The solenoid must be carefully wound to keep the windings constant in order to maintain the constant magnetic field within.

A problem with bending the solenoid is that a gradient can be introduced in the magnetic field. The gradient in the magnetic field causes the Larmor radius to be larger where the magnetic field is smaller, which can be seen in the definition of the Larmor radius [12]:

$$r_L \equiv \frac{m v_{\perp}}{|q| B} \quad (5.1)$$

The drift velocity of the positrons can be derived from the Lorentz equation and is found to be [12]:

$$v_{\nabla B} = \frac{1}{2} v_{\perp} r_L \frac{\vec{B} \times \nabla \vec{B}}{|\vec{B}|^2} \quad (5.2)$$

What Equation 5.2 signifies is that the positrons will drift away from the plane which contains the axial magnetic field and the gradient, i.e. perpendicular to the curve in the beam. This could cause the positrons to impact the drift lens. The solution is to use a gentle curve in the beam to minimize the magnetic field gradient or to have a bend followed by a section with a straight lens and solenoid.

### 5.2.2 Remoderation

The brightness per volt of a positron beam can be considered more important than the intensity of a beam or the flux. Brightness can be thought of as the number of positrons of a particular energy per second per unit cross sectional area. Positrons emitted from a moderator tend to have a large cross sectional area. The beam could be focused simply using electrostatic or magnetic means, but the brightness is never increased and usually reduced because a wide range of energy is now contained in a small area. To increase the brightness, the beam is accelerated to keV energies and focused on a secondary moderator. As described

earlier, energetic positrons implant and thermalize. Positrons then have the possibility to be re-emitted normally to the surface with energy equal to the positron work function of the moderator. The intensity of the re-emitted beam is only reduced to 20 to 30% of that incident on the secondary moderator, although the cross sectional area can be decreased by two to three orders of magnitude, therefore significantly increasing the brightness in one step [6].

## References

- [1] Goddard, Peter, ed, *Paul Dirac: The Man and His Work*, New York: Cambridge University Press, 1998.
- [2] Krause-Rehberg, Reinhard, and Hartmut S. Leipner, *Positron Annihilation in Semiconductors: Defect Studies*, Berlin: Springer-Verlag, 1999.
- [3] Charlton, Michael, and Humberston, J.W., *Positron Physics*, New York: Cambridge University Press, 2001.
- [4] *Eric Wiesstein's World of Physics*. Ed. Eric W. Weisstein. 22 February 2005. Wolfram Research. March 2005 <<http://scienceworld.wolfram.com/physics/>>.
- [5] Seijbel, Leendert Joost, "An instrument for Positron Micro-analysis," Ph.D. Dissertation, Technische Universiteit Delft, Netherlands, 1995.
- [6] Coleman, Paul. ed, *Positron Beams: and Their Applications*, New York: World Scientific, 2000.
- [7] *DePAC Tutorials*. Ed. Plochow-Besch, H., 28 Jan 2000, Received. Grupin, C. 21 Jan. 2000, Universität Siegen, March 2005, <[http://besch2.physik.uni-siegen.de/~depac/DePAC/DePAC\\_tutorial\\_database/grupen\\_istanbul/node9.html](http://besch2.physik.uni-siegen.de/~depac/DePAC/DePAC_tutorial_database/grupen_istanbul/node9.html)>.
- [8] Hautojärvi, Pekka. Ed, *Positrons in Solids*, New York: Springer-Verlag, 1979.
- [9] Tipler, Paul A., and Ralph A. Llewellyn., *Modern Physics*, 4th ed, New York: W.H. Freeman and Company, 2003.
- [10] Krane, Kenneth S., *Introductory Nuclear Physics*, New York: John Wiley & Sons, 1998.
- [11] Szilagy, Miklos, *Electron and Ion Optics*, New York: Plenum Press, 1988.
- [12] Chen, Francis F., *Introduction to Plasma Physics and Controlled Fusion*, New York: Plenum Press, 1988.
- [13] Skalsey, Mark, "A Pair Production Based Slow Positron Beam," Unpublished report, Final Report—Michigan Memorial Phoenix Project Grant, Michigan Positron Group, University of Michigan, 2004.
- [14] "NCSU PULSTAR Reactor," Unpublished report, North Carolina State University, Raleigh North Carolina. n.d.
- [15] *Visitors Guide to the NCSU Pulstar Reactor*, Raleigh, NC, n.p., n.d.

- [16] X-5 Monte Carlo Team, "MCNP5—A General Monte Carlo N-Particle Transport Code, Version 5," Los Alamos National Laboratory, Los Alamos, NM, Tech. Rep. LA-UR-03-1987, 2003.
- [17] *The Isotopes Project Home Page*, Ed. Firestone, Richard B, 4 Apr. 2001, Lawrence Berkley National Lab, Thermal Neutron Capture Homepage, April 2005, <<http://isotopes.lbl.gov/>>.
- [18] van Veen, A., et. al., "Intense Positron Sources and their Application," *Material Science Forum*, vols. 363-365, pg. 415-419, 2001.
- [19] *National Nuclear Data Center*, Nuclear Reaction Databases, ENDF, Brookhaven National Laboratory, April 2005, <<http://www.nndc.bnl.gov/index.jsp>>.
- [20] Dahl, David A., *SIMION 3D Version 7.0 User's Manual*, Idaho Falls, ID, Idaho National Engineering and Environmental Laboratory, 2000.
- [21] Gidley, David, Conversation Michigan Positron Group, University of Michigan, June 2004.
- [22] Skalsey, Mark, "Estimates of Induced Radioactivity in the NCSU Prototype Positron Beam: A Guide to Designers", Unpublished report, Michigan Positron Group, University of Michigan, June 2004.
- [23] Faw, Richard E., and J. Kenneth Shultis, *Radiological Assessment: Sources and Doses*, La Grange Park, IL, American Nuclear Society, Inc., 1999.
- [24] K. Hagiwara et al, (Particle Data Group). *Phys. Rev. D* **66**, 010001 (2002)
- [25] Baylis, William E., *Electrodynamics: A Modern Geometric Approach*, Boston: Birkhäuser, 1999.
- [26] Serway, Raymond A., and Robert J. Beichner, *Physics for Scientists and Engineers: with Modern Physics*, Vol. 2., 5th ed., n.p.: Harcourt College Publishers, n.d.
- [27] Knoll, Glen F., *Radiation Detection and Measurement*, 3rd ed., New York: John Wiley & Sons, Inc., 1999.
- [28] LaMarsh, John R., and Anthony J. Baratta, *Introduction to Nuclear Engineering*, 3rd ed., Upper Saddle River, New Jersey: Prentice Hall, 2001.
- [29] Baum, Edward M., Harold D. Knox and Thomas R. Miller, *Nuclides and Isotopes: Chart of the Nuclides*. 16th ed., n.p.: KAPL, Lockheed Martin Distribution Services, 2002.

- [30] Perry, Robert H., and Don W. Green, *Perry's Chemical Engineers' Handbook*. 7th ed., New York: McGraw-Hill, 1997.

# **Appendices**

## Appendix A

To harden and intensify the high energy photon flux across beam tube 6, photon production from thermal neutron capture reactions in materials with high neutron absorption cross sections can be utilized. A material search was performed to determine what material would produce the most intense photon production above 1-MeV. A list of prompt gamma rays produced from neutron capture reactions was obtained from The Isotopes Project Home Page, run by Lawrence Berkley National Lab.<sup>7</sup> This list contains the energy of the emitted gamma rays, the (n, $\gamma$ ) cross section, and the gamma-ray emission intensity of a particular nuclide. This list had to be sorted to determine the optimum material to use.

The rate equation for neutron interactions, or the number of collisions a neutron experiences, is shown in Equation A.1:

$$R = N\sigma\phi \quad (\text{A.1})$$

where R is the rate of interactions,  $\sigma$  is the spectral averaged cross section, N is the number density of the target atoms and  $\phi$  is the neutron flux.<sup>8</sup> The probability for a particular gamma emission to occur can be determined by dividing the reaction rate by the number density of the target nuclei and multiplying by the intensity of emission, as seen below.

$$\Gamma\left(\frac{R}{N}\right) = \Gamma\sigma\phi \quad (\text{A.2})$$

Because the neutron flux across the beam tube would be identical regardless of the material used, to determine the optimum material, the element list should be sorted based on the product of the cross section of a particular reaction and the gamma emission intensity.

Table A.1 shows just the top 200 prompt gammas of the more that 18,000 listed with energy above 1MeV based on the sorting method mentioned above. As can be seen, isotopes of Gadolinium seem to offer the greatest intensity of gamma rays above 1MeV. Cadmium can also be seen frequently in the top 200 as well. Cadmium was chosen over Gadolinium for the prototype because stock material was already available. Gadolinium can be used in future work to further optimize the performance of the beam.

---

<sup>7</sup> *The Isotopes Project Home Page*, Ed. Firestone, Richard B, 4 Apr. 2001, Lawrence Berkley National Lab, Thermal Neutron Capture Homepage, April 2005, <http://isotopes.lbl.gov/>.

<sup>8</sup> LaMarsh, John R., and Anthony J. Baratta, *Introduction to Nuclear Engineering*, 3rd ed., Upper Saddle River, New Jersey: Prentice Hall, 2001.

**Table A. 1.** Partial sorting of prompt gamma rays based on product of flux and intensity

Isotope	Z	Energy_Text	Energy	XS_Text	Cross Section	Br_Text	Intensity	$\sigma\Gamma$
158-Gd	64	1107.612(9)	1107.612	1830(40)	1830	35.3(8)	3.53E+01	6.46E+04
158-Gd	64	1185.988(9)	1185.988	1600(90)	1600	30.8(17)	3.08E+01	4.93E+04
158-Gd	64	1187.122(9)	1187.122	1420(90)	1420	27.4(17)	2.74E+01	3.89E+04
158-Gd	64	1119.163(10)	1119.163	1180(30)	1180	22.7(6)	2.27E+01	2.68E+04
158-Gd	64	6750.11(5)	6750.11	965(30)	965	18.6(6)	1.86E+01	1.79E+04
158-Gd	64	1183.968(10)	1183.968	958(60)	958	18.5(12)	1.85E+01	1.77E+04
158-Gd	64	1097.002(10)	1097.002	662(15)	662	12.8(3)	1.28E+01	8.47E+03
158-Gd	64	1323.387(10)	1323.387	641(16)	641	12.4(3)	1.24E+01	7.95E+03
158-Gd	64	1263.478(10)	1263.478	641(15)	641	12.4(3)	1.24E+01	7.95E+03
158-Gd	64	1141.458(10)	1141.458	530(30)	530	10.2(6)	1.02E+01	5.41E+03
156-Gd	64	1158.986(12)	1158.986	490(150)	490	9(3)	9.44E+00	4.63E+03
158-Gd	64	5903.39(6)	5903.39	457(14)	457	8.8(3)	8.81E+00	4.03E+03
158-Gd	64	1116.624(12)	1116.624	419(9)	419	8.07(17)	8.07E+00	3.38E+03
158-Gd	64	1259.837(9)	1259.837	417(10)	417	8.04(19)	8.04E+00	3.35E+03
156-Gd	64	1065.136(12)	1065.136	410(120)	410	7.9(23)	7.90E+00	3.24E+03
158-Gd	64	1004.058(9)	1004.058	404(22)	404	7.8(4)	7.79E+00	3.15E+03
156-Gd	64	1230.789(23)	1230.789	390(120)	390	7.5(23)	7.52E+00	2.93E+03
156-Gd	64	1187.120(21)	1187.12	340(100)	340	6.6(19)	6.55E+00	2.23E+03
158-Gd	64	1327.154(9)	1327.154	294(9)	294	5.67(17)	5.67E+00	1.67E+03
156-Gd	64	1154.102(12)	1154.102	290(170)	290	6(3)	5.59E+00	1.62E+03
158-Gd	64	1437.910(10)	1437.91	276(10)	276	5.32(19)	5.32E+00	1.47E+03
158-Gd	64	1219.947(9)	1219.947	242(12)	242	4.66(23)	4.66E+00	1.13E+03
158-Gd	64	4925.25(13)	4925.25	235(8)	235	4.53(15)	4.53E+00	1.06E+03
158-Gd	64	1010.19(3)	1010.19	232(7)	232	4.47(13)	4.47E+00	1.04E+03
150-Sm	62	1170.59(4)	1170.59	230(10)	230	4.64(20)	4.64E+00	1.07E+03

Isotope	Z	Energy_Text	Energy	XS_Text	Cross Section	Br_Text	Intensity	$\sigma\phi$
158-Gd	64	1278.932(9)	1278.932	228(12)	228	4.39(23)	4.39E+00	1.00E+03
158-Gd	64	1180.328(9)	1180.328	223(21)	223	4.3(4)	4.30E+00	9.59E+02
158-Gd	64	1517.419(10)	1517.419	219(18)	219	4.2(4)	4.22E+00	9.24E+02
158-Gd	64	1301.093(9)	1301.093	213(6)	213	4.10(12)	4.10E+00	8.73E+02
156-Gd	64	1040.430(12)	1040.43	209(60)	209	4.0(12)	4.03E+00	8.42E+02
158-Gd	64	1237.625(9)	1237.625	208(9)	208	4.01(17)	4.01E+00	8.34E+02
156-Gd	64	1242.481(17)	1242.481	204(60)	204	3.9(12)	3.93E+00	8.02E+02
158-Gd	64	1372.805(10)	1372.805	195(15)	195	3.8(3)	3.76E+00	7.33E+02
156-Gd	64	1180.36(4)	1180.36	189(60)	189	3.6(12)	3.64E+00	6.88E+02
158-Gd	64	1944.269(20)	1944.269	181(24)	181	3.5(5)	3.49E+00	6.32E+02
156-Gd	64	1277.508(18)	1277.508	180(50)	180	3.5(10)	3.47E+00	6.25E+02
158-Gd	64	1956.29(12)	1956.29	175(21)	175	3.4(4)	3.37E+00	5.90E+02
156-Gd	64	1067.185(12)	1067.185	160(50)	160	3.1(10)	3.08E+00	4.93E+02
158-Gd	64	2180.474(22)	2180.474	159(50)	159	3.1(10)	3.06E+00	4.87E+02
158-Gd	64	5582.26(15)	5582.26	155(6)	155	2.99(12)	2.99E+00	4.63E+02
158-Gd	64	2203.51(11)	2203.51	151(10)	151	2.91(19)	2.91E+00	4.39E+02
158-Gd	64	1856.41(3)	1856.41	147(50)	147	2.8(10)	2.83E+00	4.16E+02
158-Gd	64	2314.82(12)	2314.82	142(6)	142	2.74(12)	2.74E+00	3.89E+02
158-Gd	64	1034.45(4)	1034.45	142(5)	142	2.74(10)	2.74E+00	3.89E+02
156-Gd	64	1168.874(13)	1168.874	140(40)	140	2.7(8)	2.70E+00	3.78E+02
156-Gd	64	1222.349(12)	1222.349	139(40)	139	2.7(8)	2.68E+00	3.73E+02
158-Gd	64	5677.28(5)	5677.28	138(15)	138	2.7(3)	2.66E+00	3.67E+02
158-Gd	64	6419.82(5)	6419.82	131(6)	131	2.52(12)	2.52E+00	3.30E+02
158-Gd	64	5661.19(16)	5661.19	124(5)	124	2.39(10)	2.39E+00	2.96E+02
114-Cd	48	1364.30(4)	1364.3	123.0(21)	123	3.32(6)	3.32E+00	4.08E+02
114-Cd	48	1209.65(4)	1209.65	122.0(19)	122	3.29(5)	3.29E+00	4.01E+02

Isotope	Z	Energy_Text	Energy	XS_Text	Cross Section	Br_Text	Intensity	$\sigma\phi$
158-Gd	64	1774.37(12)	1774.37	122(40)	122	2.4(8)	2.35E+00	2.87E+02
158-Gd	64	5403.38(20)	5403.38	120(5)	120	2.31(10)	2.31E+00	2.77E+02
158-Gd	64	2196.56(16)	2196.56	120(12)	120	2.31(23)	2.31E+00	2.77E+02
158-Gd	64	2702.34(14)	2702.34	116(5)	116	2.24(10)	2.24E+00	2.60E+02
158-Gd	64	2023.778(20)	2023.778	114(30)	114	2.2(6)	2.20E+00	2.51E+02
156-Gd	64	1250.637(21)	1250.637	113(30)	113	2.2(6)	2.18E+00	2.46E+02
158-Gd	64	5542.93(12)	5542.93	112(5)	112	2.16(10)	2.16E+00	2.42E+02
158-Gd	64	5179.16(16)	5179.16	110(6)	110	2.12(12)	2.12E+00	2.33E+02
156-Gd	64	1174.058(13)	1174.058	110(30)	110	2.1(6)	2.12E+00	2.33E+02
158-Gd	64	1255.980(10)	1255.98	109(4)	109	2.10(8)	2.10E+00	2.29E+02
156-Gd	64	1682.081(19)	1682.081	108(30)	108	2.1(6)	2.08E+00	2.25E+02
158-Gd	64	1530.279(12)	1530.279	107(8)	107	2.06(15)	2.06E+00	2.20E+02
150-Sm	62	1193.84(4)	1193.84	106(3)	106	2.14(6)	2.14E+00	2.27E+02
156-Gd	64	1449.849(21)	1449.849	106(30)	106	2.0(6)	2.04E+00	2.16E+02
158-Gd	64	5784.15(5)	5784.15	105(5)	105	2.02(10)	2.02E+00	2.12E+02
158-Gd	64	5058.37(17)	5058.37	105(5)	105	2.02(10)	2.02E+00	2.12E+02
158-Gd	64	1663.561(11)	1663.561	105(8)	105	2.02(15)	2.02E+00	2.12E+02
158-Gd	64	1587.806(10)	1587.806	105(4)	105	2.02(8)	2.02E+00	2.12E+02
158-Gd	64	1007.340(20)	1007.34	105(4)	105	2.02(8)	2.02E+00	2.12E+02
158-Gd	64	5250.2(4)	5250.2	103(17)	103	2.0(3)	1.98E+00	2.04E+02
158-Gd	64	3989.3(4)	3989.3	103(22)	103	2.0(4)	1.98E+00	2.04E+02
158-Gd	64	2678.60(16)	2678.6	101(20)	101	1.9(4)	1.95E+00	1.97E+02
158-Gd	64	1405.877(10)	1405.877	101(4)	101	1.95(8)	1.95E+00	1.97E+02
158-Gd	64	2617.93(16)	2617.93	100(6)	100	1.93(12)	1.93E+00	1.93E+02
158-Gd	64	2577.32(15)	2577.32	100(6)	100	1.93(12)	1.93E+00	1.93E+02
158-Gd	64	3700.3(4)	3700.3	99(17)	99	1.9(3)	1.91E+00	1.89E+02

Isotope	Z	Energy_Text	Energy	XS_Text	Cross Section	Br_Text	Intensity	$\sigma\phi$
114-Cd	48	1399.54(4)	1399.54	97.7(15)	97.7	2.63(4)	2.63E+00	2.57E+02
156-Gd	64	1366.473(18)	1366.473	97(30)	97	1.9(6)	1.87E+00	1.81E+02
150-Sm	62	1350.39(5)	1350.39	94(12)	94	1.89(24)	1.89E+00	1.78E+02
158-Gd	64	1000.859(10)	1000.859	93(4)	93	1.79(8)	1.79E+00	1.66E+02
158-Gd	64	2259.983(23)	2259.983	92(6)	92	1.77(12)	1.77E+00	1.63E+02
158-Gd	64	1815.045(11)	1815.045	92(20)	92	1.8(4)	1.77E+00	1.63E+02
158-Gd	64	5592.95(21)	5592.95	91(4)	91	1.75(8)	1.75E+00	1.59E+02
158-Gd	64	1781.711(10)	1781.711	91(22)	91	1.8(4)	1.75E+00	1.59E+02
158-Gd	64	2515.41(20)	2515.41	88(6)	88	1.70(12)	1.70E+00	1.50E+02
158-Gd	64	1692.30(6)	1692.3	88(13)	88	1.70(25)	1.70E+00	1.50E+02
114-Cd	48	2455.93(7)	2455.93	87.3(18)	87.3	2.35(5)	2.35E+00	2.05E+02
158-Gd	64	2799.39(17)	2799.39	87(7)	87	1.68(13)	1.68E+00	1.46E+02
158-Gd	64	1377.86(8)	1377.86	87(5)	87	1.68(10)	1.68E+00	1.46E+02
156-Gd	64	1079.25(3)	1079.25	87(30)	87	1.7(6)	1.68E+00	1.46E+02
158-Gd	64	2073.593(11)	2073.593	84(7)	84	1.62(13)	1.62E+00	1.36E+02
158-Gd	64	6671.73(5)	6671.73	83(4)	83	1.60(8)	1.60E+00	1.33E+02
158-Gd	64	5239.83(17)	5239.83	83(10)	83	1.60(19)	1.60E+00	1.33E+02
158-Gd	64	3520.6(3)	3520.6	83(9)	83	1.60(17)	1.60E+00	1.33E+02
158-Gd	64	1145.225(9)	1145.225	82(9)	82	1.58(17)	1.58E+00	1.30E+02
156-Gd	64	1965.970(25)	1965.97	80(25)	80	1.5(5)	1.54E+00	1.23E+02
150-Sm	62	1321.95(7)	1321.95	76(9)	76	1.53(18)	1.53E+00	1.16E+02
158-Gd	64	4310.0(3)	4310	76(5)	76	1.46(10)	1.46E+00	1.11E+02